Chromosome segregation in *Escherichia coli* involves DNA binding by the MinC-MinD complex

Navaneethan Palanisamy[*,1,#], Linda Klauss[*,1,§], Maïween Lefebvre[1], Jungsheng Liang[1], Götz Hofhaus[2], Johan Zeelen[3], Maximilian Urban[4], Mehmet Ali Öztürk[1], Sabine Merker[5], Marcin Luzarowski[5], Thomas Ruppert[5] and Barbara Di Ventura[1,6,&]

[1] Institute of Biology II, Faculty of Biology, University of Freiburg, Freiburg, Germany

[2] Center for Quantitative Biology (BioQuant), University of Heidelberg, Heidelberg, Germany

[3] German Cancer Research Center (DKFZ), Heidelberg, Germany

[4] Ludwig-Maximilians-Universität München (LMU), Munich, Germany

[5] Core Facility for Mass Spectrometry and Proteomics, Center for Molecular Biology of Heidelberg University (ZMBH), DKFZ-ZMBH Alliance, 69120 Heidelberg, Germany

[6] Signalling Research Centres BIOSS and CIBSS, University of Freiburg, Freiburg, Germany

[#] current address: Chester Medical School, University of Chester, Chester, UK

[§] current address: Gyros Protein Technologies AB, Uppsala, Sweden

[&] Correspondence to: Barbara Di Ventura; barbara.diventura@bio.uni-freiburg.de

* These authors contributed equally

Abstract

The *Escherichia coli* Min system, composed of the proteins MinC, MinD, and MinE, is crucial for directing septum formation at mid-cell. MinD has also been implicated in chromosome segregation due to its non-sequence-specific DNA binding ability. Here, we demonstrate that the MinCD complex, rather than MinD alone, is the primary driver of Min-mediated chromosome segregation and that MinE regulates the transient nature of this interaction. We further reveal a critical function for the linker connecting MinC's N- and C-terminal domains

in both DNA binding and FtsZ polymerization inhibition. *E. coli* strains expressing MinC linker variants from the native locus exhibit chromosome segregation defects. The defects are more pronounced in strains where the nucleoid-associated protein HU is endogenously tagged with GFP. These findings reinforce the involvement of the Min system in chromosome segregation in *E. coli* and highlight a previously unrecognized role for the MinC linker.

Introduction

E. coli cells divide by constriction of the cell wall by a contractile ring structure called the Z-ring. This structure is made of polymers of FtsZ, a conserved GTPase that shares structural similarity with eukaryotic tubulin[1, 2]. In the absence of FtsZ's spatial regulators, the Z-ring would form anywhere in the cell. To inhibit Z-ring formation at the poles and over the nucleoid two machineries are at place in *E. coli*: the Min system and the nucleoid occlusion[3]. Other still unclear mechanisms additionally ensure mid-cell determination in this bacterium[4, 5]. The nucleoid occlusion mechanism is put in action by the protein SlmA, which binds DNA at specific sites scattered along the chromosome with the exception of the terminus-containing region and inhibits FtsZ polymerization there[6, 7]. The Min system comprises three proteins: MinC, MinD and MinE. It owes its name from the observation that *E. coli* strains having mutations in or deletion of the operon encoding these proteins –the *minB* operon– divide asymmetrically giving rise to miniaturized cells deprived of chromosomal DNA[8, 9]. These round, chromosome-less cells have been denominated minicells and the proteins forming the machinery that ensures symmetric cell division and absence of minicells were called Min proteins, and together the Min system.

MinC is a potent inhibitor of FtsZ polymerization. While it is able to do so on its own, a 25-50 times higher cellular concentration of MinC is needed to antagonize FtsZ efficiently in the absence of MinD[10]. Indeed, MinC is *per se* a cytoplasmic protein and, if expressed in the

54 absence of MinD and MinE, it is simply diffused throughout the cell, thus requiring high
55 concentrations to counteract FtsZ, which is instead tethered to the cytoplasmic membrane by
56 its binding partners FtsA and ZapA[11-13]. Thanks to its association with MinD, an ATPase that
57 associates with the cytoplasmic membrane through its C-terminal amphipathic helix (also
58 called a membrane-targeting sequence or MTS)[14-17], MinC gets in close proximity to FtsZ and
59 can potently destabilize its polymers even at endogenous expression levels. MinC is composed
60 of two functional domains: an N-terminal domain ($MinC^N$) and a C-terminal domain ($MinC^C$)
61 connected by a linker allowing flexibility in the orientation of $MinC^N$[18, 19]. The boundaries of
62 these domains are not universally defined. Some reports define $MinC^N$ as the region of the
63 protein comprising amino acids 1-120, while $MinC^C$ as comprising amino acids 127-231[20];
64 others state $MinC^N$ to comprise amino acids 1-115 of MinC and $MinC^C$ to include amino acids
65 116-231[21]. So far, nothing is known about the role of this linker except that it imparts flexibility
66 between the two domains of MinC. No mutations in this region are known to impair MinC's
67 functionality. $MinC^C$ contains a dimerization domain and interacts directly with MinD[22]. When
68 in complex with MinD, $MinC^C$ interacts with the C-terminal tail of FtsZ, which is also involved
69 in the interaction with FtsA and ZapA[23], thus competing with these proteins and finally
70 destabilizing and disrupting the Z-ring[23, 24]. $MinC^N$ is also dimeric due to a so-called domain
71 swap, whereby the first beta-strand of each monomer belongs to a beta-sheet located on the
72 other monomer[25]. $MinC^N$ is a stronger FtsZ antagonist than $MinC^C$. It attacks and shortens FtsZ
73 polymers without affecting FtsZ's GTPase activity[21]. Taken together, it can be concluded that
74 MinC binds to FtsZ and destabilizes its polymers with both its N- and C-terminal domains[18,
75 26].
76 MinD forms ATP-dependent dimers[27]. Although ADP-bound monomeric MinD can associate
77 with the cytoplasmic membrane via its MTS, this interaction is weak. When in dimeric form,
78 the interaction becomes stable[14]. In the absence of MinE or when expressed at much higher

levels than MinE, MinD decorates the whole cytoplasmic membrane. MinE is recruited to the membrane by membrane-bound MinD, which triggers a conformational change in MinE that exposes a previously cryptic MTS, which allows MinE to also directly associate with the membrane[28]. Subsequently, MinE stimulates the ATPase activity of MinD, which leads to the dissociation of the MinD dimer and the release of MinD from the membrane[29, 30]. In the cytoplasm, ADP is exchanged with ATP, and ATP-bound MinD rebinds to the membrane at locations where MinE concentration is the lowest, that is, the opposite pole. This reaction-diffusion mechanism leads to oscillations of MinD/MinE from one cell pole to the other[31, 32]. MinE and MinC compete for the same binding surface on MinD[33]. As a matter of fact, MinE displaces MinC from MinD before activating MinD's ATPase activity[27, 34-36].

Beyond its role in Z-ring positioning, the Min system has been implicated in chromosome segregation[37]. MinD was shown to bind DNA *in vitro* in a non-sequence-specific manner[37]. A mutant MinD capable of DNA binding, but unable to bind to the membrane, was shown to co-localize with the nucleoid in living *E. coli* cells[37]. Interestingly, MinD was found to bind to the DNA and the membrane at the same time, an essential feature for the mechanism of chromosome segregation that was put forward[37]. Later, the DNA-binding protein Noc, the actuator of the nucleoid occlusion mechanism in *Bacillus subtilis*, was also shown to bind simultaneously to the membrane and the DNA, thus suggesting that such "dual binders" might be more widespread than previously anticipated[38]. MinD is part of the ParA-MinD family of ATPases[39]. Members of this family are known to bind DNA to perform either plasmid or chromosome segregation in various organisms[40]. MinD has been seen for a long time as the exception, due to the fact that it was believed to bind to the membrane only and not to DNA and to be responsible for mid-cell determination, but not chromosome segregation. *E. coli,* however, does not possess a chromosomal Par system. The Min-mediated mechanism of

104 chromosome segregation involves repeated, transient DNA-membrane tethering events, which
105 impede the random backward movement of the duplicated chromosomes toward mid-cell[37].
106 This proposed mechanism still requires entropic forces to separate the duplicated chromosomes
107 at the beginning of the cell cycle. Once these forces become weaker due to the increased
108 physical separation of the duplicated chromosomes, the Min-mediated mechanism becomes
109 important to keep them away from mid-cell, each close to one pole.
110 So far, only MinD-DNA interaction was directly studied by various biochemical assays and
111 fluorescence microscopy in living *E. coli* cells[37]. Here we investigate the interaction of MinC
112 and MinE with DNA, alone or when together with the other Min proteins. We show that the
113 MinCD complex is the primary DNA-binding entity within the Min system, and that MinE and
114 FtsZ (at high concentrations) interfere with the binding. We find that the linker connecting
115 $MinC^N$ and $MinC^C$ is essential for MinCD-DNA binding, which is abolished *in vitro* by even
116 small perturbations to it. The linker is also important for MinC's function towards FtsZ. Using
117 the CRISPR/Cas9 and Lambda Red recombineering, we construct MG1655 and MG1655-
118 HUαGFP (Fishov)[40] strains expressing MinC linker mutants from the endogenous locus. All
119 strains have some degree of chromosome segregation defects, which become particularly
120 pronounced in the Fishov strain.
121 Together, these data corroborate the role of the Min system in chromosome segregation under
122 physiological conditions and reveal an unexpected role for the MinC linker in the binding to
123 DNA.
124
125 **Results**
126 **The MinCD complex binds DNA *in vitro***
127 To test the ability of MinC, alone and with MinD, to bind to DNA, we cloned the *minC* and
128 *minD* genes in pET28a and purified the 6xHis-T7-tagged proteins from *E. coli* Rosetta cells

129 using Nickel-based affinity chromatography. We then performed electrophoretic mobility shift
130 assays (EMSAs) using a fluorescently labeled 30 bp DNA fragment. While MinC and MinD
131 alone bound DNA extremely weakly (Supplementary Fig. 1a,b), the MinCD complex bound
132 DNA strongly, in a concentration-dependent manner in the presence of ATP (Supplementary
133 Fig. 1b). When we used a longer DNA fragment (120 bp), we found that His-MinC at 2 μM
134 could also shift all the DNA probe (Supplementary Fig. 1c), albeit in this case the nucleoprotein
135 complex was found mostly in the well and not into the gel, as seen for the sample with MinC
136 and MinD (Supplementary Fig. 1d).
137 These EMSAs were performed with the His-tagged proteins. To test if the His-tag could
138 influence the binding, we removed it from both proteins using thrombin and performed the
139 EMSAs again (note that the T7 tag is still present at the N-terminus of the proteins). We found
140 that, indeed, both proteins had reduced DNA binding in the absence of the His-tag, yet the
141 binding was still strong when using both proteins together, especially when using a longer
142 DNA probe (Supplementary Fig. 1e and Fig. 1a). We decided to perform all further
143 experiments with purified proteins from which the His-tag was removed.
144 Titrating the proteins one at a time with a 52 bp DNA probe we saw that, when having MinD
145 at 4 μM, 1 μM MinC was sufficient to shift the vast majority of the DNA probe (Fig. 1a), while,
146 when having MinC at 4 μM, 4 μM MinD were necessary to observe a similar strong binding
147 (Fig. 1b). When we used a longer DNA probe, we observed the same pattern, although in this
148 case, 2 μM MinD were sufficient to shift all the DNA probe (Supplementary Fig. 1f,g). Taken
149 together, these data indicate that MinC has higher affinity for the DNA than MinD, although
150 this affinity is still rather weak when MinC is alone. In the presence of MinD, the affinity for
151 the DNA increases several folds. The concentration-dependent binding of the MinCD complex
152 with DNA was observed with probes of various lengths (Fig. 1c).

153 To confirm the results of the EMSA, we performed a liposome co-sedimentation assay in the
154 presence of plasmid DNA. We found that the plasmid DNA co-sedimented with the liposomes
155 when MinC and MinD were mixed together with ATP (Fig. 1d, lane 3, upper panel). The
156 MinCD-DNA complex was partially found in the pellet even in the absence of the liposomes
157 (Fig. 1d, lane 2, upper panel). In the presence of ADP, there was only a very weak signal for
158 the DNA in the pellet (Fig. 1d, lane 5, upper panel). While this could be due to binding to MinD
159 alone, considering that there was hardly any DNA in the pellet of the sample with only MinD
160 (Fig. 1d, lane 1, upper panel), we speculate the weak signal is rather due to some residual
161 MinCD complex in the pellet of the sample with ADP (Fig. 1d, lane 5, middle panel). When
162 the non-hydrolysable ATP-analogue ATP-γS was used instead of ATP, we found a decreased
163 amount of DNA in the pellet (Fig. 1d, lane 4, upper panel). Looking at the amount of MinC
164 and MinD in the pellet/supernatant (Fig. 1d, lane 4, middle panel), we conclude that ATP-γS
165 affects the binding between MinC and MinD more than the MinD-liposome interaction, leading
166 to reduced DNA binding. These results indicate that the MinCD complex is capable of binding
167 DNA while being associated with the membrane.
168

169 **In the presence of DNA, the MinCD co-polymers assemble *in vitro* into sheets whose width**
170 **is proportional to the length of the DNA fragment**

171 The results of the liposome co-sedimentation assay, which showed that a fraction of the
172 MinCD-DNA complex goes to the pellet even in the absence of liposomes, suggest that the
173 proteins form a high-molecular weight complex with the DNA. This is also evident in the
174 EMSAs, where the signal is often found in or very close to the well. To more directly observe
175 these structures, we performed negative-stain transmission electron microscopy. Upon
176 incubation of MinC, MinD, ATP and DNA, we observed the formation of sheets (Fig. 2a). We
177 believe these sheets are formed by a number of the previously reported MinCD co-polymers[41,

[42]. Using DNA fragments of different lengths as well as plasmid DNA, we found that the width of the sheets is proportional to the length of the DNA fragment used in the experiment (Fig. 2b). In the absence of added DNA, sheets are still visible, but they are found more sporadically (Supplementary Fig. 2).

In the experiment described above, the DNA was not directly visible. To visualize the DNA, we used 5 nm gold beads coated with poly-dT DNA via a sulfur-gold chemistry. These single-stranded fiducials (ss fiducials) were annealed with an excess of poly-dA to form double-stranded fiducials (ds fiducials). The MinCD co-polymers were formed by mixing purified MinD and MinC proteins in the presence of ATP. After the addition of the fiducials, the samples were plunge-frozen and observed in the electron microscope. We found that the ds fiducials aligned along the co-polymeric filaments in a linear way (Fig. 2c, left panel) in contrast to the random binding pattern of the ss fiducials (Fig. 2c, middle panel). This regular pattern required the presence of the MinCD filaments (Fig. 2c, right panel). The ss fiducials sometimes formed clusters, which could be reduced in number, but not eliminated by one additional heating/annealing cycle. This treatment did not affect the regular line pattern seen for the ds fiducials.

A statistical analysis of all inter-fiducial distances up to 250 pixels confirmed the visual observations. The lines of ds fiducials appear to consist of beads at defined distances, and clear peaks corresponding to multiples of this distance (manifolds) are evident in the histogram (Fig. 2c, lower left panel). In contrast, the distances between ss fiducials are random (Fig. 2c, lower middle panel). While the overall binding of ss and ds fiducials to the filaments is comparable, the ss fiducials tend to be more dispersed, resulting in fewer short-range interactions and the disappearance of the peak at the primary distance. The few clusters of ss fiducials observed in the absence of filaments also exhibit a peak at a short distance (18.5 nm), suggesting a potential

intrinsic tendency for these fiducials to form small aggregates. These results, together with our EMSA data, support the conclusion that MinC and MinD bind to double-stranded DNA, forming ordered structures.

MinE and FtsZ interfere with DNA binding by the MinCD complex

To investigate the ability of MinE to bind DNA, we cloned the *minE* gene into pET28a, and purified the 6xHis-T7-tagged protein from *E. coli* Rosetta cells using Nickel-based affinity chromatography. Also in this case, we decided to compare the binding of the His-tagged protein and of the protein after removal of the His-tag. Consistent with what was observed for MinD and MinC, the His-tag led to stronger DNA binding by MinE (Supplementary Fig. 1 and Fig. 3a). Co-incubation with MinD did not improve the binding (Fig. 3b).

Next we investigated the effect of MinE on DNA binding by the MinCD complex using the liposome co-sedimentation assay. We found that MinE interferes with DNA binding by the MinCD complex in a concentration-dependent manner (Fig. 3c). Since MinE competes with MinC for the same binding surface on MinD and dislodges MinC from MinD, it is not surprising that it leads to the dissociation of the MinC-MinD-DNA complex, which requires MinC and MinD to be in a complex.

We also tested if FtsZ would interfere or enhance DNA binding by MinCD. To this aim, we cloned the *ftsZ* gene into pET28a, purified the protein from *E. coli* Rosetta cells using Nickel-based affinity chromatography and removed the His-tag. We then performed liposome co-sedimentation assay in the presence of plasmid DNA. FtsZ was found in the pellet either when alone or when co-incubated with MinC and MinD, albeit the amount of protein in the pellet was higher for the sample with MinCD (Fig. 3d, compare lanes 3 and 4, middle panel). There was no discernible difference in the results obtained with GDP and GTP (Fig. 3d). We speculate this is due to the intrinsically high GTPase activity of FtsZ[43], which leads to the accumulation

228 of GDP in the sample that contained initially only GTP. Note that, in this assay, it is not possible
229 to discern polymers, which form in the presence of GTP, from shorter oligomers and/or
230 condensates, which form in the presence of GDP[44]. Upon incubation with 10 μM FtsZ, the
231 protein ratio MinC/FtsZ in the lipid-associated pellet was ± 2:1 and there was a small decrease
232 of DNA in the pellet (Fig. 3d, lower panel). Increasing the concentration of FtsZ to 30 μM
233 resulted in an equal amount of MinC and FtsZ in the pellet and highly reduced plasmid DNA
234 in the pellet (Fig. 3d, lower panel). Since FtsZ binds to both the N- and the C-terminal domains
235 of MinC, it most likely prevents DNA binding by blocking the binding sites on MinC (and
236 possibly MinD). We confirmed that FtsZ interferes with the DNA binding by the MinCD
237 complex using EMSA (Fig. 3e). Already two minutes of incubation were sufficient to prevent
238 all binding.
239
240 **The linker connecting MinC N- and C-terminal domains is needed for DNA binding with**
241 **MinD and affects the activity of MinC towards FtsZ**
242 Integrating the data obtained so far with the previously suggested role of the Min system in
243 chromosome segregation[37], we conclude that the real effector of the system in this process is
244 the MinCD complex and not MinD. As chromosome segregation defects were observed before
245 only in an *E. coli* strain overexpressing from plasmid a mutant MinD, we aimed to investigate
246 if chromosome segregation defects would be evident when expressing at endogenous, thus
247 physiological levels a mutant Min protein unable to bind DNA. To draw conclusions about
248 chromosome segregation defects due to failed DNA binding by MinCD rather than to
249 morphological issues, we needed a mutant protein (either MinC or MinD) affected only in its
250 ability to bind DNA, but retaining all other functionalities. Such a mutant would allow us to
251 study chromosome segregation in cells with otherwise normal Z-ring positioning. Since MinC
252 has the highest DNA binding affinity, and considering that MinD has to perform more activities

253 than MinC (interact with the membrane, MinC, and MinE, and hydrolyze ATP to oscillate from
254 pole to pole), we decided to focus on MinC. MinC is, as mentioned above, composed of two
255 domains separated by a linker (Fig. 4a). We decided to test the role of this linker in DNA
256 binding. We predicted that it would not be important for the binding to MinD, since this
257 happens via $MinC^{C}$[22]. We expected it, however, to play a role in MinC's activity towards FtsZ,
258 since both MinC domains destabilize FtsZ polymers and their correct positioning towards FtsZ
259 might be important[18, 26]. The linker region of MinC is always referred to as "flexible", because
260 attempts to crystallize full-length MinC failed so far and, for *T. maritima* MinC, two
261 orientations of $MinC^{N}$ were found in the crystals, which was taken as a proof of the flexibility
262 of the linker[19]. Looking at two available crystal structures of MinC N and C-terminal domains,
263 we found that, in the isolated $MinC^{N}$, only residues 1-101 are resolved[25], and that, in the
264 isolated $MinC^{C}$, residues 121-231 are resolved[45]. This suggests that the linker region comprises
265 amino acids 102-120 (Fig. 4b). Interestingly, it is composed of several amino acids that are
266 found in rigid linkers such as alanine, lysine, and proline[46]; indeed, it is predicted to be rigid
267 by the MEDUSA web server[47]. Nonetheless, given the known flexibility between $MinC^{N}$ and
268 $MinC^{C}$ afforded by the linker, we decided to substitute it with flexible linkers made of various
269 repeats of glycine and serine. We cloned and purified the following MinC linker mutants: GS,
270 1x AGGSG, 2x AGGSG, 3x AGGSG, 4x AGGSG, and 19RL (Fig. 4b). In the GS construct,
271 $MinC^{N}$ and $MinC^{C}$ are separated by two amino acids, namely glycine (G) and serine (S). In the
272 1x AGGSG construct (from now on, 1x), the linker region comprises five amino acids, namely
273 alanine (A), glycine (G), glycine (G), serine (S) and glycine (G). In the 2x mutant, this sequence
274 is repeated twice, and so on. The linker in the 19RL mutant is identical to that in the 4x mutant,
275 but lacks the last glycine. Therefore, this mutant linker is as long as MinC's native linker (that
276 is, it is 19 amino acid long). We then performed EMSAs with wild-type and mutant MinC
277 proteins. We found that all linker variants lost their ability to bind DNA with MinD *in vitro*

278 (Fig. 4c). To investigate the importance of the length of the linker without changing its amino
279 acid sequence, we also constructed mutants of MinC carrying truncations of the linker (Fig.
280 4d). These mutant MinC proteins were also unable to bind DNA with MinD *in vitro* (Fig. 4e).
281 The linker seems, therefore, crucial for DNA binding. To test the role of the linker further, we
282 investigated the DNA binding ability of the isolated $MinC^{C}$ containing the linker (Fig. 4f, upper
283 panel). This protein bound the DNA with MinD even better than full-length MinC (Fig. 4f,
284 lower panel).
285 We confirmed that all the MinC linker mutants were not affected in their ability to bind to
286 MinD and be recruited to the liposomes (Supplementary Fig. 3). For the flexible linker mutants
287 (1x-4x), we additionally checked that they could be dislodged off MinD by MinE
288 (Supplementary Fig. 4). These results corroborate our assumption that the linker is not involved
289 in the binding of MinC to MinD and MinE.
290 Finally, we investigated the ability of the linker mutants and truncations to destabilize FtsZ
291 polymers using the spot assay. We expressed either MinC (WT, linker truncations and mutants)
292 alone under the strong IPTG-inducible T7 promoter in *E. coli* Rosetta cells (Fig. 4g, upper
293 panel), or together with MinD under the arabinose-inducible P_{BAD} promoter in MG1655ΔminB
294 cells (Fig. 4h, upper panel). When overexpressed alone, all the linker variants were impaired
295 in their interaction with FtsZ (Fig. 4g, lower panel). In the presence of MinD, the activity
296 towards FstZ improved for all but the GS linker mutant, whose overexpression did not cause
297 filamentation and consequently cell death (Fig. 4h, lower panel). Despite being somewhat
298 affected in their activity towards FtsZ, MinC linker mutants are able to block Z-ring formation
299 when overexpressed with MinD (leading to cell filamentation and cell death), thus they
300 represent a viable option to investigate the impact of DNA binding on chromosome segregation
301 in living cells for which Z-ring positioning by the Min system is likely in place.
302

303 ***E. coli* strains expressing MinC linker mutants from the endogenous locus show**
304 **chromosome segregation defects**

305 To construct strains expressing MinC linker mutants at endogenous levels, we applied a
306 genome engineering method based on the CRISPR/Cas9 and the Lambda Red recombination
307 systems[48], which allowed us to swap the native linker with the 1x-4x variants directly at the
308 endogenous locus. We used two donor strains: MG1655 and MG1655 where a *gfp* gene is
309 inserted in frame downstream of endogenous *hupA* (Fishov strain)[49]. This strain, therefore,
310 expresses the fusion of the alpha subunit of HU (HUα) with GFP and allows visualization of
311 the nucleoid without the use of further stains (e.g. DAPI). Since the procedure itself might
312 affect the cells, we additionally constructed a silent mutant of MinC in both genetic
313 backgrounds. In these strains, only the nucleotide sequence of the linker was mutated with
314 alternative codons for the same amino acids. Consequently, they both express wild-type MinC.
315 As a first characterization of the strains, we measured growth curves in LB and M9 media. We
316 found that all mutant strains, including those expressing the silent mutant, grew less than the
317 wild type (Fig. 5a). The 1x linker mutant grew less than all other mutants, for both strains and
318 in both media. Nonetheless, the difference in growth was very moderate.

319 We then measured cell length using the automated software BacStalk[50]. Note that, in this
320 measurement, minicells were explicitly excluded. We found a statistically significant
321 difference between the wild type and almost each mutant, with the exception of the 2x linker
322 mutant in the MG1655 background and the 4x linker mutant in the Fishov background (Fig.
323 5b). In the MG1655 background, the median was almost identical in all strains (Fig. 5b, upper
324 panel). In the Fishov background, the silent mutant, as well as the 2x and 3x mutants gave rise
325 to smaller cells than the wild type (Fig. 5b, lower panel). The 1x mutant, despite having a
326 similar median as the wild type, had many longer cells.

327 To look directly at chromosome segregation, we employed fluorescence microscopy using
328 DAPI to stain the nucleoid and constructed demographs of the DAPI signal (Fig. 5c,d). Note
329 that, albeit the Fishov strains express HUα-GFP, we opted for staining them also with DAPI
330 because, after fixation, the GFP signal was too weak. Moreover, we wanted to treat all samples
331 in the same way. Observation of the demographs with the naked eye revealed a clear defect for
332 several of the mutants in the Fishov background (Fig. 5d, lower panel). To resolve defects not
333 obvious to the naked eye, we decided to calculate a measure that would indicate the spread of
334 the DAPI signal in the cell. For less well segregated chromosomes, we expect a higher spread.
335 We therefore calculated the ratio between the number of black pixels (which indicate the area
336 of the cell without DNA) and the total number of pixels in the cell. We calculated the average
337 of this ratio for all cells and expressed it as a percentage (Fig. 5e,f). With this measure, it is
338 possible to appreciate that even in the MG1655 background there are chromosome segregation
339 defects, especially for the silent, 2x and 3x mutants (Fig. 5e). Nonetheless, clearly the defects
340 are much more pronounced in the Fishov background (Fig. 5f).
341
342 **Discussion**
343 The role of the Min system in mid-cell determination and Z-ring positioning is well established.
344 However, its contribution to chromosome segregation has been less acknowledged. One reason
345 for this might be the fact that, when the involvement of the Min system in chromosome
346 segregation was first proposed, the roles of MinC and MinE had not been studied, and
347 chromosome segregation defects had been shown only in MG1655Δ*minB* cells overexpressing
348 a mutant MinD with decreased DNA binding from plasmid[37]. Here we clarified the role of
349 MinC and MinE, showing that the real actuator driving chromosome segregation is the MinCD
350 complex, while MinE ensures that the binding is transient. Moreover, we used CRISPR/Cas9
351 coupled with the Lambda Red recombination to construct strains that are identical to the

352 parental ones except that endogeous MinC carries a modified linker, which we demonstrated
353 to abrogate DNA binding *in vitro*. Using these strains, we demonstrated chromosome
354 segregation defects for some of the linker mutants, with particularly severe defects in cells
355 expressing a GFP-tagged version of the alpha subunit of the histone-like protein HU. This could
356 be due to the fact that HU plays a role in maitaining the correct structure of the chromosome
357 and the fusion to GFP may not be as functional as the wild-type and therefore this strain may
358 already suffer from mild defects in chromosome structure/compaction or other processes
359 related to HU[51-54]. Indeed, comparison of demographs for wild-type strains shows better
360 separation in MG1655 than in MG1655::*huα-gfp* (Fig. 5c,d). These mild defects are
361 exacerbated in the MinC linker mutant strains.
362 As mentioned already, the mutant strains in the MG1655 background show only minor defects.
363 While the DNA binding activity of the mutants was assessed *in vitro*, translating these results
364 to the cellular context is challenging due to the complexity of cellular environments, including
365 varying protein concentrations and additional factors. It is possible that the mutations partially
366 impair DNA binding in the cell, leading to milder defects than observed *in vitro*.
367
368 It is difficult to entirely disentagle the activity of the Min system towards FstZ and in
369 chromosome segregation because, if altered, both processes lead to the formation of minicells.
370 As a matter of fact, there are several reports stating the presence of minicells as a consequence
371 of failed chromosome segregation[55-59]. By taking snapshots of all the constructed strains in the
372 microscope and quantifying the percentage of minicells formed, we found that, in the MG1655
373 background, all the linker mutants produced minicells compared to the wild-type strain and the
374 strain expressing the silent mutant, with the 2x linker mutant producing the highest amount of
375 minicells, followed closely by the 3x mutant (Supplementary Fig. 6). While this is consistent
376 with the segregation defects for these mutants (Fig. 5e), there is a discrepancy for the silent

377 mutant, which produces no minicells despite having the strongest segregation defects. The
378 same trend is found in the Fishov backround, although in this case the percentage of minicells
379 produced by the linker mutants is overall higher (Supplementary Fig. 7). Nonetheless, cells
380 with chromosome segregation issues may fail to divide all together, which could explain why
381 minicells are not formed. The demograph (Fig. 5d) and the cell length calculation (Fig. 5b,
382 lower panel) indicate that Fishov strain cells expressing the 1x mutant are much longer than
383 wild-type Fishov strain cells.
384 We were surprised to find differences between wild-type strains and those with silent mutations
385 in MinC linker. We excluded the possibility that these differences are due to protein levels
386 (Supplementary Fig. 8). Therefore, the phenotypic effects might be caused by the presence of
387 regulatory elements like small RNAs, which need further investigation in the future.
388
389 The electron microscopy results reveal that the DNA is bound by the MinCD co-polymers (Fig.
390 2). When using free dsDNA fragments, we observed sheets with widths proportional to the
391 DNA length, suggesting that DNA runs perpendicular or at an angle to the filaments. In
392 contrast, when using dsDNA fiducials attached to gold beads, these aligned along single
393 filaments without connecting neighbouring filaments. The linear arrangement of the beads
394 seems to follow the curved filaments and hardly switch to a neighboring filament. In fact,
395 neighboring filaments are hardly labeled at all. This also points to a cooperativity: the binding
396 of the first bead facilitates the binding of the following bead to the same filament, leading to
397 the formation of lines on selected filaments. Individual beads bound to filaments are rare. Such
398 cooperative binding could be advantageous during segregation, as MinCD filaments attached
399 to replicated chromosomes might bind increasingly stronger to longer streches, pulling these
400 stretches towards the cell poles. Albeit the role of the MinCD co-polymers in living cells has
401 been debated[60], it cannot be excluded they indeed form. We speculate that these filaments

402 might more effectively retain segregated chromosomes at the poles, leaving the mid-cell free
403 for the cytokinetic ring.
404
405 **Materials and methods**
406 **Strains and growth conditions**
407 The strains used in this study are listed in Supplementary Table 1. The *E. coli* TOP10 strain
408 was used for cloning, and the *E. coli* Rosetta™(DE3)pLysS (Novagen) strain was used for
409 overproduction and protein purification. All *E. coli* strains were grown in LB or M9 + 0.4%
410 glucose supplemented with the appropriate antibiotic(s) at 37 ºC with shaking.
411
412 **Construction of plasmids**
413 pET28a-MinD and pET28a-MinE plasmids were constructed as previously described[37, 61]. The
414 *minC* gene was amplified from *E. coli* MG1655 genomic DNA using *BamHI*_MinC_FP and
415 *NotI*_MinC_RP primers. The amplicon and pET28a empty plasmid were double digested using
416 *BamHI* and *NotI* and then ligated to get pET28a-MinC. Similarly, the *ftsZ* gene was amplified
417 from *E. coli* MG1655 genomic DNA using *BamHI*_FtsZ_FP and *HindIII*_FtsZ_RP primers.
418 The amplicon and pET28a empty plasmid were double digested using *BamHI* and *HindIII* and
419 then ligated to get pET28a-FtsZ. pET28a-MinC-GS was obtained by amplifying the whole
420 pET28a-MinC plasmid except the linker region (i.e., residues 102 to 120) using phosphorylated
421 primers MinC_GS_FP and MinC101_RP with the forward primer containing the codons for
422 "GS", and then self-circularizing the linear PCR product using T4 DNA ligase. Using the same
423 strategy and same reverse primer (i.e., MinC101_RP), pET28a-MinC-1xAGGSG (using
424 primer MinC_1xAGGSG_FP), pET28a-MinC-2xAGGSG (using primer
425 MinC_2xAGGSG_FP), pET28a-MinC-3xAGGSG (using primer MinC_3xAGGSG_FP),
426 pET28a-MinC-4xAGGSG (using primer MinC_4xAGGSG_FP), pET28a-MinC19RL (using

427 primer MinC_19RL_FP), pET28a-MinC-Δ4 (using primer MinC_del4_FP), pET28a-MinC-Δ8
428 (using primer MinC_del8_FP) and pET28a-MinC-Δ13 (using primer MinC_del13_FP) were
429 constructed. Also, using the same strategy, pET28a-MinC$^{C+linker}$ (using primers MinC102_FP
430 and pET28a_*BamHI*_RP) was constructed.
431 pBAD33-MinCD was obtained from a previously constructed pBAD33-MinCDE[61] by
432 removing the *minE* gene by linearization and self-circularization using phosphorylated primers
433 pBAD33_*HindIII*_FP and MinD_RP. Using the same strategy and primers mentioned above
434 for pET28a-MinC linker variants, pBAD33-MinCD-GS, pBAD33-MinCD-1xAGGSG,
435 pBAD33-MinCD-2xAGGSG, pBAD33-MinCD-3xAGGSG, pBAD33-MinCD-4xAGGSG,
436 pBAD33-MinCD-Δ4, pBAD33-MinCD-Δ8 and pBAD33-MinCD-Δ13 were constructed.
437 For all the PCR amplifications, high-fidelity Phusion polymerase (New England Biolabs) was
438 used. Plasmids were amplified by transforming them into chemically competent *E. coli* TOP10
439 cells (Invitrogen™) and were isolated using the QIAprep® Spin Miniprep Kit (Qiagen) as per
440 the manufacturer's protocol. The constructs were validated via Sanger sequencing (GATC
441 Biotech, Germany). The list of primers used in this study is given in Supplementary Table 2.
442
443 **Constructions of strains with MinC linker variants**
444 To generate strains expressing MinC linker mutants from the endogenous locus we employed
445 a method combining CRISPR/Cas9 and Lambda red homologous recombination[48]. The two
446 plasmids, pcas9 and pTarget (Lambda Red Homologous Recombination Plasmid and CRISPR
447 HR gRNA Plasmid), were purchased from Sigma-Aldrich. pcas9 was transformed into wild-
448 type *E. coli* MG1655 and the cells were plated on LB agar plates with 50 μg/mL kanamycin.
449 The strain harbouring pcas9 was cultured overnight in LB medium at 30°C with shaking (250
450 r.p.m.). The next day, a fresh culture was started from the overnight culture using 3 mL fresh
451 LB medium with 50 μg/mL kanamycin. The culture was then grown at 30°C until the OD_{600}

452 reached 0.3-0.5. 1.5% arabinose was used to induce the expression of the Lambda red
453 recombination proteins for 1 hour. Cells were then collected and washed twice with 40 μL ice-
454 cold 20% glycerol to make them become electrocompetent. Donor DNA and pTarget were
455 transformed into the cells by electroporation. Cells bearing both pcas9 and pTarget were
456 selected on LB agar plates with 50 μg/mL kanamycin and 100μg/mL ampicillin. The donor
457 DNA was obtained by PCR using high-fidelity Phusion polymerase (ThermoFisher). After
458 electroporation, the cells were plated on LB agar plates with 50 μg/mL kanamycin and
459 100μg/mL ampicillin. A randomly selected colony for each strain was picked from the plate
460 and a PCR was performed to check for the presence of the mutations. This colony was grown
461 overnight and then a diluted culture was spread on a LB agar plate with 5% saccharose. The
462 plate was left overnight at 37 °C. The following morning, eight colonies for each strain were
463 randomly selected and streaked onto three plates: a LB agar plate with no antibiotic, a LB agar
464 plate with 100 μg/mL ampicillin, and a LB agar plate with 50 μg/mL kanamycin. The plates
465 were incubated overnight at 37 °C. The next day, the colonies that died on the plates with the
466 antibiotics were considered cured of pCas9 and pTarget and were therefore selected by using
467 the LB plate without antibiotic. The correctness of the sequence of every MinC linker mutant
468 was checked by colony PCR followed by Sanger sequencing.
469
470 **Protein purification**
471 Protein purifications were performed as previously described[37] with minor modifications.
472 Rosetta cells carrying the desired plasmid were grown to an OD600 of 0.5-0.9 and induced
473 with 1 mM IPTG for 3 hours at 37 °C. Cells were collected by centrifugation (4.000-5.000
474 r.p.m.) at 4 °C for 20 minutes and stored at -20 °C. Pellets were thawed on ice and resuspended
475 in lysis buffer. The buffers used in this study are listed in Supplementary Table 3. Cells were
476 then lysed by sonication and the crude lysate was clarified by centrifugation (20.000 r.p.m.) for

477 20 min at 4 °C. Proteins were purified using the Profinia™ Protein Purification System (Bio-
478 Rad), with a BIO-RAD® Bio-Scale™ Mini Profinity™ IMAC Cartridge (1 mL) and the BIO-
479 RAD® Bio-Scale™ Mini Bio-Gel® P-6 Desalting Cartridge (10 mL). The column was washed
480 with imidazole buffer and the protein was eluted with elution buffer, followed by exchange of
481 the elution buffer for storage buffer. The purified proteins were stored in small aliquots at -80
482 °C. Protein concentrations were estimated based on the absorbance at 280 nm with a NanoDrop
483 spectrophotometer (Thermo Scientific). Proteins were cleared from any aggregates by
484 centrifugation (21.000 g) for 30 min at 4 °C prior to use.
485
486 **Elimination of the His-tag**
487 His-tag cleavage was performed for the other aliquot by incubating the proteins with thrombin
488 agarose beads (Thrombin CleanCleave™ Kit from Sigma-Aldrich) for 3 hours at room
489 temperature on a rotating wheel. After the His-tag removal, the proteins were stored at -80 °C
490 in 50 μL aliquots.
491
492 **Electrophoretic mobility shift assays**
493 Proteins were incubated with 50 nM 5' HEX-labelled (hexachloro-6-carboxy-fluoresceine)
494 DNA in a buffer containing 50 mM HEPES-KOH pH 7.25, 150 mM KCl, 10 % glycerol, 0.1
495 mM EDTA pH 8.0, 1 mM ADP/ATP and 5 mM $MgCl_2$ at room temperature for 10 min. The
496 reaction mixture was then loaded on a 6 % native-PAGE gel. The gel was run in 0.5x TBE
497 buffer for 20 min at constant voltage (150 V). Finally, the gel image was obtained using an
498 Amersham Typhoon Gel and Blot Imaging Systems (GE Healthcare).
499
500 **Preparation of double-stranded DNA probes for EMSAs**

501 Two complementary oligos were mixed in NEB buffer 2 and the mixture was heated up to
502 98°C in a heat block. After 2 minutes, the heat block was switched off, and the samples were
503 left to gradually cool down. DNA probes longer than 120 bp were amplified via PCR using a
504 forward primer with a HEX label, followed by gel purification of the fragment using the Qiagen
505 PCR clean up kit.
506
507 **Liposome preparation**
508 *E. coli* total lipids (powder) were purchased from Avanti Polar Lipids. The lipids were
509 dissolved in liposome buffer (20 mM HEPES pH 7.5, 150 mM NaCl and 5 mM β-
510 mercaptoethanol) to a final concentration of 20 mg/mL and left for 30 minutes at 37 °C. For
511 better hydration, the sample was frozen in liquid nitrogen and heated up to 37 °C in a heat
512 block a total of 5 times. Lipid vesicles were obtained using the Avanti Mini Extruser with a
513 200 nm filter. The sample was passed through the filter 20 times, aliquoted and stored at -80
514 °C.
515
516 **Liposome co-sedimentation assay**
517 We used a previously described protocol[37]. Liposomes (320 µg/mL in Figs. 1d and 3 c,d, 500
518 µg/mL in Supplementary Fig. 3 and 160 µg/mL in Supplementary Fig. 4) were incubated for
519 10 min with the proteins (6 µM MinC and MinD in Figs. 1d and 3 c,d, 2 µM MinC and MinD
520 in Supplementary Fig. 3, and 1 µM MinC and MinD in Supplementary Fig. 4) and 1 mM of
521 either ADP or ATP in 50 µL reaction volume in ATPase buffer (25 mM Tris-HCl, pH 7.5, 50
522 mM KCl, 5 mM MgCl2, 5% glycerol). The reactions were pelleted by centrifugation at 21.000
523 g for 15-30 min, the pellets were resuspended in 50 µL ATPase buffer, and supernatant and
524 pellet samples were analyzed by SDS-PAGE, followed by Coomassie staining to detect the
525 proteins.

Liposome co-sedimentation in the presence of plasmid DNA

Purified proteins (varying concentrations) were incubated with 800 µg/mL liposomes, 32 ng/µL plasmid DNA and 1 mM ADP/ATP in storage buffer supplemented with 5 mM $MgCl_2$. After 15 minutes of incubation at room temperature, the reaction mixture was spun down in a table top centrifuge at 21.000 g for 20 minutes. The supernatant was removed and mixed in a 1:1 ratio with 2x Laemli buffer. The pellet was dissolved in 1x Laemli buffer with a volume matching that of the supernatant. After heating the samples for 5 minutes at 95 °C, the protein content of pellet and supernatant fractions was analysed with SDS-page followed by Coomassie staining. A 1% agarose gel stained with Gel Red™ Nucleic Acid Stain was used to analyse the DNA content. The intensity of the DNA and protein bands was quantified with ImageJ.

Negative-stain transmission electron microscopy

The filaments were formed by incubating MinC (4 µM) with MinD (4 µM), 1 mM ATP, 10 mM MgCl2 and DNA (50 nM) for 15 minutes on ice. Grids with continuous carbon were glow discharged and 3 µl of sample were pipetted on the grid. After 30 seconds, the liquid was removed and 10 µl of 1% uranyl acetate in water were pipetted on the grid and incubated for 30 seconds. The excess stain was removed and the grids were dried. For each condition 25 images were randomly taken and the number of filaments in the sheets determined. Single filaments were not counted.

Preparation of DNA fiducials

Single-stranded fiducials (ss fiducials) were prepared by coating citrate gold beads of 5 nm (PROVIDER) with thiolated single-stranded dT DNA oligomers (HOW LONG?). To obtain

551 double-stranded fiducials (ds fiducials), an excess of dA oligomers (HOW LONG?) was added
552 and annealed to the ss fiducials.
553
554 **Binding of DNA fiducials to MinCD co-polymers**
555 MinCD co-polymeric filaments were produced by mixing 4 μM of MinD with 4 μM MinC.
556 Larger aggregates were removed by spinning the protein solutions at 15 000 x g for 30 minutes.
557 Polymerization was started by adding ATP (200 μM final concentration) and $MgCl_2$ (10 mM
558 final concentration) and incubating the mixture for 10 minutes on ice. An equal volume of the
559 fiducials was added and the 3 μl of the sample was plunge-frozen on Quantifoli grids (0.6/1,
560 2/1, 3.5/1) with blotting times between 5 and 15 seconds at 100% humidity. Grids were
561 observed in a Krios instrument (Thermo Fisher) and screened at low magnification (135x) to
562 identify good quality regions. Best grids were selected for targeted imaging (Latitude/Gatan)
563 or random imaging (EPU/FEI). For the analysis, 2x binned images were used at a pixel size of
564 2.74 Å. After manual exclusion of low-quality images, the gold beads were localized
565 (imodfindbeads) and all linear distances computed (imod-dist) with an ad-hoc script
566 (Supplementary Information). Occurring instances smaller than 250 pixels were counted (in
567 125 bins for smoothing the data) and plotted.
568
569 **Heat treatment of ds fiducials**
570 ds fiducials were heated to 95 °C and cooled to 4 °C over 30 minutes.
571
572 **Spot assay**
573 Spot assay was performed as previously described[16]. Briefly, the plasmids were transformed
574 into either *E. coli* ROSETTA or MG1655Δ*minB* strain. A colony was picked and suspended in
575 a nutrient broth without any antibiotic. The cells were then serially diluted and spotted on agar

576 plates with different IPTG or arabinose concentration. The plates were then incubated
577 overnight at 37 °C and imaged using a gel imaging system (Analytik Jena).
578
579 **Growth curve measurement**
580 Each strain was grown overnight at 37°C and shaken at 200 rpm in the selected medium (either
581 LB or M9 + 0.4% glucose). The cultures were diluted to OD_{600}=0.1 and added in triplicates to
582 a 96-well microplate. The OD_{600} of each well was measured every 10 minutes for 24 hours by
583 the CLARIOstar® Plus Microplate Reader from BMG labtech. The microplate was incubated
584 at 37°C and shaken before every measurement. The experiment was repeated three times.
585
586 **Cell length measurement**
587 The *E. coli* MG1655 and Fishov strains were grown overnight at 37°C and shaken at 200 rpm
588 in M9 + 0.4% glucose medium. The morning after, cultures were diluted to OD_{600}=0.1 and
589 incubated in the same conditions for 4 hours. After reaching an OD_{600} of approximately 0.4,
590 bacteria were fixed with a 37 % formaldehyde solution in PBS. 100 nM DAPI were added to
591 each sample prior to microscopy analysis. Microscopy pictures were taken on a Zeiss Axio
592 Observer Z1/7 (Carl Zeiss Microscopy). 3 µL of the bacteria-containing solution were spread
593 on a 1% agarose pad on metal microscope slides. The BacStalk software[50] was used to detect
594 cells and automatically measure their length. The size and position of nucleiods in the cells
595 were determined with the MicrobeJ plugin of ImageJ by measuring the intensity of the DAPI
596 fluorescence throughout the whole length of the bacteria.
597
598 **Demographs**
599 The demographs were created using the MicrobeJ plugin of ImageJ. Cells with a length
600 between 1.5 and 6 µm were selected using the selection parameters of the software. The cells

601 were sorted by cell length in ascending order from top to bottom. Only the pixels with a
602 fluorescence intensity greater than 0.7 were plotted to increase the readability of the graphs.
603
604 **Sample preparation for mass spectrometry**
605 An overnight culture of each mutant strain, plus the parental strains, was grown in LB at 37°C
606 and shaken at 200 r.p.m. The morning after, a fresh culture of 2 mL was started with OD_{600}=0.1,
607 and let grown at 37 °C and shaken at 200 r.p.m. for two hours. The cultures were then pelleted
608 at maximal speed in a table-top centrifuge. The pellet was resuspended in 4x Laemli buffer
609 diluted in PBS (to obtain 1x Laemli buffer) and boiled at 98 °C for ten minutes. The samples
610 were then loaded on a SDS gel, which, after the run, was stained with Coomassie and sent over
611 for mass spectrometry analysis.
612
613 **Mass spectrometry**
614 **In-gel tryptic digestion**
615 Upon SDS-PAGE, Coomassie-stained bands were manually excised from the gel and
616 processed as described before[62]. Two gel slices covering theoretical molecular weight from ±
617 18 kDa up to 37 kDa were collected per gel lane. The extracted peptides from each gel slice
618 were analyzed using LC-MS/MS, generating separate raw data files for each slice.
619
620 **LC-MS/MS analysis**
621 Nanoflow LC-MS^2 analysis was performed with an Ultimate 3000 liquid chromatography
622 system coupled to an Orbitrap QE HF (Thermo Fisher). An in-house packed analytical column
623 (75 µm x 200 mm, 1.9 µm ReprosilPur-AQ 120 C18 material (Dr. Maisch, Germany) was used.
624 Mobile phase solutions were prepared as follows, solvent A: 0.1% formic acid / 1% acetonitrile,
625 solvent B: 0.1% formic acid, 89.9% acetonitrile. Peptides were separated in a 60 min linear

626 gradient started from 3% B and increased to 23% B over 50 min and to 38% B over 10 min,
627 followed by washout with 95% B. The mass spectrometer was operated in data-dependent
628 acquisition mode, automatically switching between MS and MS2. MS spectra (m/z 400–1600)
629 were acquired in the Orbitrap at 60,000 (m/z 400) resolution and MS2 spectra were generated
630 for up to 15 precursors with a normalized collision energy of 27 and an isolation width of 1.4
631 m/z.
632
633 **Database search and data processing**
634 The MS/MS spectra were searched against the Swiss-Prot *Saccharomyces cerevisiae*
635 (UP000002311, November 2019) and *Escherichia coli (*UP000000625, November 2019)
636 protein databases and a customized contaminant database (part of MaxQuant, MPI Martinsried)
637 using Proteome Discoverer 2.5 with Sequest HT (Thermo Fisher Scientific). A fragment ion
638 mass tolerance was set to 0.02 Da and a parent ion mass tolerance to 5 ppm. Trypsin was
639 specified as an enzyme. Carbamidomethyl was set as fixed modification of cysteine and
640 oxidation (methionine), and deamidation (asparagine, glutamine) as variable modifications of
641 peptides. Acetylation, methionine-loss, and a combination of acetylation and methionine-loss
642 were set as variable modifications of the protein terminus. For feature linking and mapping,
643 RT tolerance [min] and mass tolerance [ppm] were set to 0.001 and 0.0005, respectively.
644 Peptide quantification was done using a precursor ion quantifier node with the Top N Average
645 method (N=3) set for protein abundance calculation. For each protein, the intensities recorded
646 in the two gel slices were summed to obtain the total protein abundance. This summation
647 approach was applied to account for any distribution of proteins between the gel slices. To
648 account for the measurement inconsistencies, median normalization was applied.
649
650 **Statistics**

651 Statistical analyses were performed in Origin Pro.

652

653 **Acknowledgments**

654 We thank Victor Sourjik (MPI, Marburg) for critical reading of this manuscript, Luis Serrano
655 (CRG, Barcelona) and Victor Sourjik for discussions during the course of this work, and Chris
656 Van der Does (University of Freiburg) for the generous donation of liposomes. We
657 acknowledge the technical support of Core Facility for Mass Spectrometry and Proteomics of
658 Center for Molecular Biology (ZMBH) of Heidelberg University. Core Facility for Mass
659 Spectrometry and Proteomics is funded by the ZMBH and partially funded by the
660 CellNetworks Core Technology Platform (CCTP) of Heidelberg University. The CCTP is
661 funded in part by the Federal Ministry of Education and Research (BMBF) and the Ministry of
662 Science Baden Württemberg within the framework of the Excellence Strategy of the Federal
663 and State Governments of Germany. Part of this work was performed at the Center for
664 Quantitative Biology (BioQuant), Heidelberg. L.K. and N.P. were funded by the German
665 Research Foundation (DFG) (grant no. VE776/2-1 to B.D.V.).

666

667 **Contributions**

668 B.D.V. conceived the study. N.P. and L.K. purified the proteins, performed EMSAs and
669 liposome co-sedimentations. N.P. performed the spot assays. J.L. constructed the mutant
670 strains and prepared the samples for mass spectrometry. M.L. characterized the strains in terms
671 of growth, cell length and chromosome segregation. G.H. and J.Z. performed all the negative-
672 stain transmission microscopy. M.U. provided the DNA fiducials. M.A.Ö. helped with
673 structural analyses. S.M., M.L and T.R. performed mass spectrometry and data analysis.
674 B.D.V. supervised the work of N.P., L.K., M.L. and J.L., provided the funding and wrote the
675 manuscript. All authors commented on and approved of the manuscript.

676

677 **References**

678 1. Erickson, H.P. FtsZ, a prokaryotic homolog of tubulin? *Cell* **80**, 367-370 (1995).

679 2. de Pereda, J.M., Leynadier, D., Evangelio, J.A., Chacon, P. & Andreu, J.M. Tubulin
680 secondary structure analysis, limited proteolysis sites, and homology to FtsZ.
681 *Biochemistry* **35**, 14203-14215 (1996).

682 3. Rothfield, L., Taghbalout, A. & Shih, Y.L. Spatial control of bacterial division-site
683 placement. *Nat Rev Microbiol* **3**, 959-968 (2005).

684 4. Cambridge, J., Blinkova, A., Magnan, D., Bates, D. & Walker, J.R. A replication-
685 inhibited unsegregated nucleoid at mid-cell blocks Z-ring formation and cell division
686 independently of SOS and the SlmA nucleoid occlusion protein in Escherichia coli. *J*
687 *Bacteriol* **196**, 36-49 (2014).

688 5. Bailey, M.W., Bisicchia, P., Warren, B.T., Sherratt, D.J. & Mannik, J. Evidence for
689 divisome localization mechanisms independent of the Min system and SlmA in
690 Escherichia coli. *PLoS Genet* **10**, e1004504 (2014).

691 6. Cho, H., McManus, H.R., Dove, S.L. & Bernhardt, T.G. Nucleoid occlusion factor
692 SlmA is a DNA-activated FtsZ polymerization antagonist. *Proc Natl Acad Sci U S A*
693 **108**, 3773-3778 (2011).

694 7. Tonthat, N.K. *et al.* Molecular mechanism by which the nucleoid occlusion factor,
695 SlmA, keeps cytokinesis in check. *EMBO J* **30**, 154-164 (2011).

696 8. Adler, H.I., Fisher, W.D., Cohen, A. & Hardigree, A.A. MINIATURE escherichia
697 coli CELLS DEFICIENT IN DNA. *Proc Natl Acad Sci U S A* **57**, 321-326 (1967).

698 9. Davie, E., Sydnor, K. & Rothfield, L.I. Genetic basis of minicell formation in
699 Escherichia coli K-12. *J Bacteriol* **158**, 1202-1203 (1984).

700 10. de Boer, P.A., Crossley, R.E. & Rothfield, L.I. Roles of MinC and MinD in the site-
701 specific septation block mediated by the MinCDE system of Escherichia coli. *J*
702 *Bacteriol* **174**, 63-70 (1992).
703 11. Bi, E.F. & Lutkenhaus, J. FtsZ ring structure associated with division in Escherichia
704 coli. *Nature* **354**, 161-164 (1991).
705 12. Hale, C.A. & de Boer, P.A. Direct binding of FtsZ to ZipA, an essential component of
706 the septal ring structure that mediates cell division in E. coli. *Cell* **88**, 175-185 (1997).
707 13. Ma, X. *et al.* Interactions between heterologous FtsA and FtsZ proteins at the FtsZ
708 ring. *J Bacteriol* **179**, 6788-6797 (1997).
709 14. Szeto, T.H., Rowland, S.L., Habrukowich, C.L. & King, G.F. The MinD membrane
710 targeting sequence is a transplantable lipid-binding helix. *J Biol Chem* **278**, 40050-
711 40056 (2003).
712 15. Szeto, T.H., Rowland, S.L., Rothfield, L.I. & King, G.F. Membrane localization of
713 MinD is mediated by a C-terminal motif that is conserved across eubacteria, archaea,
714 and chloroplasts. *Proc Natl Acad Sci U S A* **99**, 15693-15698 (2002).
715 16. Zhou, H. & Lutkenhaus, J. Membrane binding by MinD involves insertion of
716 hydrophobic residues within the C-terminal amphipathic helix into the bilayer. *J*
717 *Bacteriol* **185**, 4326-4335 (2003).
718 17. Hu, Z. & Lutkenhaus, J. A conserved sequence at the C-terminus of MinD is required
719 for binding to the membrane and targeting MinC to the septum. *Mol Microbiol* **47**,
720 345-355 (2003).
721 18. Hu, Z. & Lutkenhaus, J. Analysis of MinC reveals two independent domains involved
722 in interaction with MinD and FtsZ. *J Bacteriol* **182**, 3965-3971 (2000).
723 19. Cordell, S.C., Anderson, R.E. & Lowe, J. Crystal structure of the bacterial cell
724 division inhibitor MinC. *EMBO J* **20**, 2454-2461 (2001).

725 20. Ramm, B., Heermann, T. & Schwille, P. The E. coli MinCDE system in the regulation
726 of protein patterns and gradients. *Cell Mol Life Sci* **76**, 4245-4273 (2019).
727 21. Shen, B. & Lutkenhaus, J. Examination of the interaction between FtsZ and MinCN
728 in E. coli suggests how MinC disrupts Z rings. *Mol Microbiol* **75**, 1285-1298 (2010).
729 22. Szeto, T.H., Rowland, S.L. & King, G.F. The dimerization function of MinC resides
730 in a structurally autonomous C-terminal domain. *J Bacteriol* **183**, 6684-6687 (2001).
731 23. Shen, B. & Lutkenhaus, J. The conserved C-terminal tail of FtsZ is required for the
732 septal localization and division inhibitory activity of MinC(C)/MinD. *Mol Microbiol*
733 **72**, 410-424 (2009).
734 24. Shiomi, D. & Margolin, W. The C-terminal domain of MinC inhibits assembly of the
735 Z ring in Escherichia coli. *J Bacteriol* **189**, 236-243 (2007).
736 25. An, J.Y. *et al.* Crystal structure of the N-terminal domain of MinC dimerized via
737 domain swapping. *J Synchrotron Radiat* **20**, 984-988 (2013).
738 26. LaBreck, C.J., Conti, J., Viola, M.G. & Camberg, J.L. MinC N- and C-Domain
739 Interactions Modulate FtsZ Assembly, Division Site Selection, and MinD-Dependent
740 Oscillation in Escherichia coli. *J Bacteriol* **201** (2019).
741 27. Wu, W., Park, K.T., Holyoak, T. & Lutkenhaus, J. Determination of the structure of
742 the MinD-ATP complex reveals the orientation of MinD on the membrane and the
743 relative location of the binding sites for MinE and MinC. *Mol Microbiol* **79**, 1515-
744 1528 (2011).
745 28. Hsieh, C.W. *et al.* Direct MinE-membrane interaction contributes to the proper
746 localization of MinDE in E. coli. *Mol Microbiol* **75**, 499-512 (2010).
747 29. Hu, Z. & Lutkenhaus, J. Topological regulation of cell division in E. coli.
748 spatiotemporal oscillation of MinD requires stimulation of its ATPase by MinE and
749 phospholipid. *Mol Cell* **7**, 1337-1343 (2001).

750 30. Lutkenhaus, J. & Sundaramoorthy, M. MinD and role of the deviant Walker A motif,
751 dimerization and membrane binding in oscillation. *Mol Microbiol* **48**, 295-303 (2003).
752 31. Hu, Z. & Lutkenhaus, J. Topological regulation of cell division in Escherichia coli
753 involves rapid pole to pole oscillation of the division inhibitor MinC under the control
754 of MinD and MinE. *Mol Microbiol* **34**, 82-90 (1999).
755 32. Raskin, D.M. & de Boer, P.A. MinDE-dependent pole-to-pole oscillation of division
756 inhibitor MinC in Escherichia coli. *J Bacteriol* **181**, 6419-6424 (1999).
757 33. Ma, L., King, G.F. & Rothfield, L. Positioning of the MinE binding site on the MinD
758 surface suggests a plausible mechanism for activation of the Escherichia coli MinD
759 ATPase during division site selection. *Mol Microbiol* **54**, 99-108 (2004).
760 34. Hu, Z., Saez, C. & Lutkenhaus, J. Recruitment of MinC, an inhibitor of Z-ring
761 formation, to the membrane in Escherichia coli: role of MinD and MinE. *J Bacteriol*
762 **185**, 196-203 (2003).
763 35. Hu, Z., Gogol, E.P. & Lutkenhaus, J. Dynamic assembly of MinD on phospholipid
764 vesicles regulated by ATP and MinE. *Proc Natl Acad Sci U S A* **99**, 6761-6766
765 (2002).
766 36. Lackner, L.L., Raskin, D.M. & de Boer, P.A. ATP-dependent interactions between
767 Escherichia coli Min proteins and the phospholipid membrane in vitro. *J Bacteriol*
768 **185**, 735-749 (2003).
769 37. Di Ventura, B. *et al.* Chromosome segregation by the Escherichia coli Min system.
770 *Mol Syst Biol* **9**, 686 (2013).
771 38. Adams, D.W., Wu, L.J. & Errington, J. Nucleoid occlusion protein Noc recruits DNA
772 to the bacterial cell membrane. *EMBO J* **34**, 491-501 (2015).
773 39. Lutkenhaus, J. The ParA/MinD family puts things in their place. *Trends Microbiol* **20**,
774 411-418 (2012).

775 40. Mierzejewska, J. & Jagura-Burdzy, G. Prokaryotic ParA-ParB-parS system links
776 bacterial chromosome segregation with the cell cycle. *Plasmid* **67**, 1-14 (2012).
777 41. Conti, J., Viola, M.G. & Camberg, J.L. The bacterial cell division regulators MinD
778 and MinC form polymers in the presence of nucleotide. *FEBS Lett* **589**, 201-206
779 (2015).
780 42. Ghosal, D., Trambaiolo, D., Amos, L.A. & Lowe, J. MinCD cell division proteins
781 form alternating copolymeric cytomotive filaments. *Nat Commun* **5**, 5341 (2014).
782 43. Mendieta, J. *et al.* Structural and functional model for ionic (K(+)/Na(+)) and pH
783 dependence of GTPase activity and polymerization of FtsZ, the prokaryotic ortholog
784 of tubulin. *J Mol Biol* **390**, 17-25 (2009).
785 44. Robles-Ramos, M.A. *et al.* Assembly of bacterial cell division protein FtsZ into
786 dynamic biomolecular condensates. *Biochim Biophys Acta Mol Cell Res* **1868**,
787 118986 (2021).
788 45. Yang, S. *et al.* Characterization of C-terminal structure of MinC and its implication in
789 evolution of bacterial cell division. *Sci Rep* **7**, 7627 (2017).
790 46. Chen, X., Zaro, J.L. & Shen, W.C. Fusion protein linkers: property, design and
791 functionality. *Adv Drug Deliv Rev* **65**, 1357-1369 (2013).
792 47. Vander Meersche, Y., Cretin, G., de Brevern, A.G., Gelly, J.C. & Galochkina, T.
793 MEDUSA: Prediction of Protein Flexibility from Sequence. *J Mol Biol* **433**, 166882
794 (2021).
795 48. Pyne, M.E., Moo-Young, M., Chung, D.A. & Chou, C.P. Coupling the CRISPR/Cas9
796 System with Lambda Red Recombineering Enables Simplified Chromosomal Gene
797 Replacement in Escherichia coli. *Appl Environ Microbiol* **81**, 5103-5114 (2015).

798 49. Abebe, A.H., Aranovich, A. & Fishov, I. HU content and dynamics in Escherichia
799 coli during the cell cycle and at different growth rates. *FEMS Microbiol Lett* **364**
800 (2017).
801 50. Hartmann, R., van Teeseling, M.C.F., Thanbichler, M. & Drescher, K. BacStalk: A
802 comprehensive and interactive image analysis software tool for bacterial cell biology.
803 *Mol Microbiol* **114**, 140-150 (2020).
804 51. Macvanin, M. & Adhya, S. Architectural organization in E. coli nucleoid. *Biochim*
805 *Biophys Acta* **1819**, 830-835 (2012).
806 52. Kuzminov, A. Bacterial nucleoid is a riddle wrapped in a mystery inside an enigma. *J*
807 *Bacteriol* **206**, e0021123 (2024).
808 53. Dame, R.T. & Goosen, N. HU: promoting or counteracting DNA compaction? *FEBS*
809 *Lett* **529**, 151-156 (2002).
810 54. Swinger, K.K. & Rice, P.A. IHF and HU: flexible architects of bent DNA. *Curr Opin*
811 *Struct Biol* **14**, 28-35 (2004).
812 55. Donovan, C., Schauss, A., Kramer, R. & Bramkamp, M. Chromosome segregation
813 impacts on cell growth and division site selection in Corynebacterium glutamicum.
814 *PLoS One* **8**, e55078 (2013).
815 56. Uhia, I. *et al.* Analysis of ParAB dynamics in mycobacteria shows active movement
816 of ParB and differential inheritance of ParA. *PLoS One* **13**, e0199316 (2018).
817 57. Pioro, M. *et al.* Competition between DivIVA and the nucleoid for ParA binding
818 promotes segrosome separation and modulates mycobacterial cell elongation. *Mol*
819 *Microbiol* **111**, 204-220 (2019).
820 58. Toro, E., Hong, S.H., McAdams, H.H. & Shapiro, L. Caulobacter requires a dedicated
821 mechanism to initiate chromosome segregation. *Proc Natl Acad Sci U S A* **105**,
822 15435-15440 (2008).

59. Bohm, K. *et al.* Chromosome organization by a conserved condensin-ParB system in the actinobacterium Corynebacterium glutamicum. *Nat Commun* **11**, 1485 (2020).

60. Park, K.T., Du, S. & Lutkenhaus, J. MinC/MinD copolymers are not required for Min function. *Mol Microbiol* **98**, 895-909 (2015).

61. Palanisamy, N., Ozturk, M.A., Akmeric, E.B. & Di Ventura, B. C-terminal eYFP fusion impairs Escherichia coli MinE function. *Open Biol* **10**, 200010 (2020).

62. Moretti-Horten, D.N. *et al.* Synchronized assembly of the oxidative phosphorylation system controls mitochondrial respiration in yeast. *Dev Cell* **59**, 1043-1057 e1048 (2024).

Figures and legends

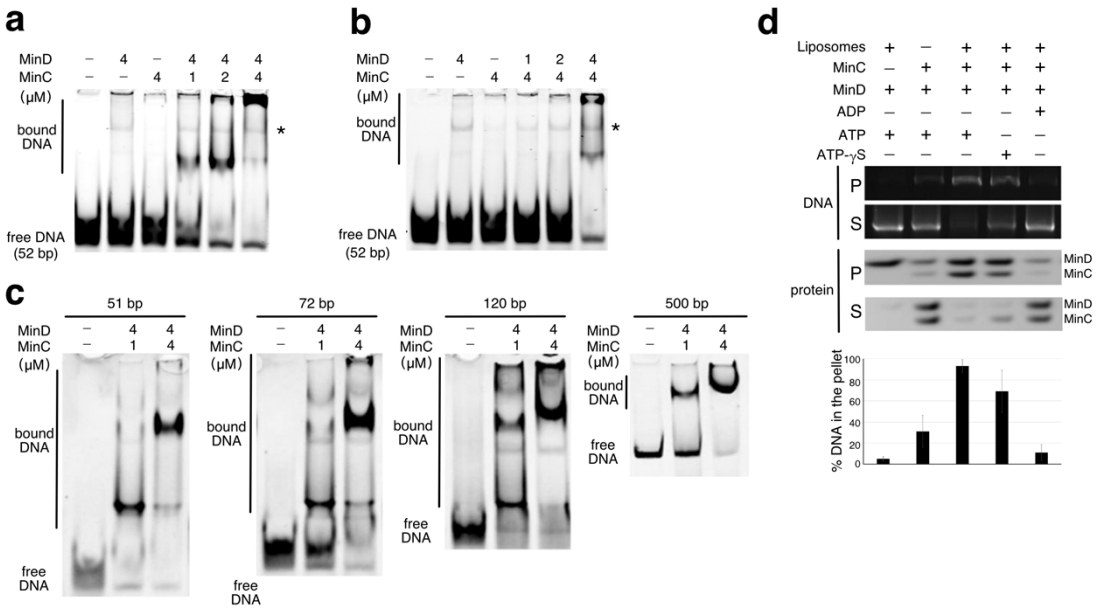

Fig 1. The MinCD complex binds DNA *in vitro*.

a-c, Electrophoretic mobility shift assays (EMSAs) performed with the indicated proteins at the indicated concentrations, and HEX-labelled DNA (50 nM) of the indicated length. All reactions were performed in the presence of 1 mM ATP. **a**,**b**, Asterisk indicates the height at which a band is visible, which is observed when incubating the DNA with MinD or MinC alone and does not represent binding by the MinCD complex. **d**, Liposome co-sedimentation assay. Upper panel, gel red-stained agarose gel used to visualize the DNA. Middle

841 panel, Coomassie-stained polyacrylamide gel used to visualize the proteins. Lower panel, bar graph showing the
842 quantification of the % of the DNA found in the pellet. Data represent mean ± S.E.M. of three independent
843 experiments. S, supernatant. P, pellet.
844

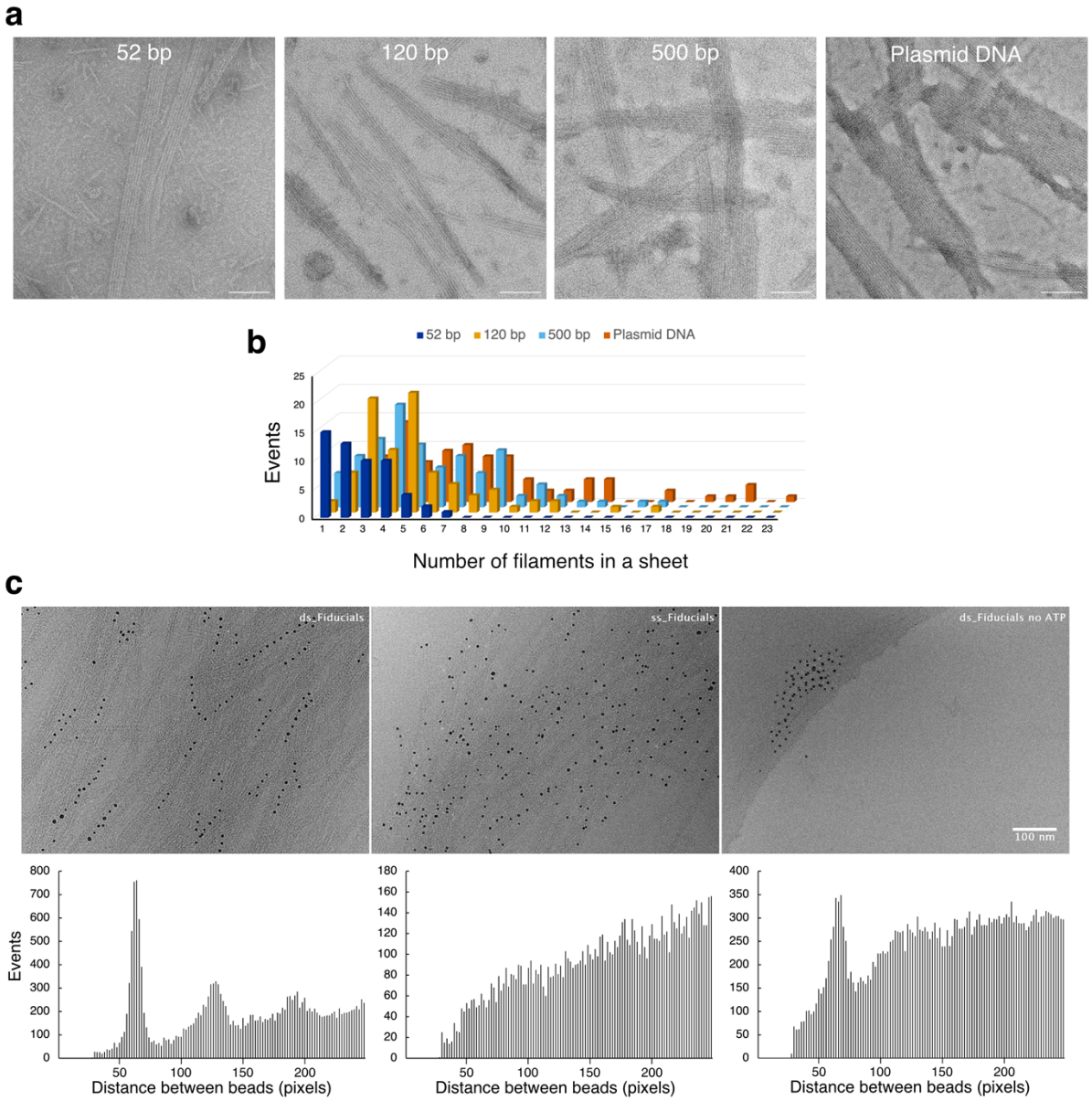

845

846 **Fig 2. The MinCD co-polymers assemble into sheets in the presence of DNA *in vitro*.**
847 **a,** Negative-stain electron-micrographs of samples containing MinC (4 μM), MinD (4 μM), 1 mM ATP, 10 mM
848 $MgCl_2$ and DNA (50 nM) of the indicated length or plasmid DNA. Scale bar, 100 nm. **b**, Bar graph showing the
849 distribution of the number of filaments per sheet for the indicated DNA fragments. **c,** Negative-stain electron-

micrographs of samples containing MinC (4 μM), MinD (4 μM), 1 mM ATP and either ds-fiducials (ds DNA) or ss-fiducials (ss DNA). Pixel size, 2.8 Å.

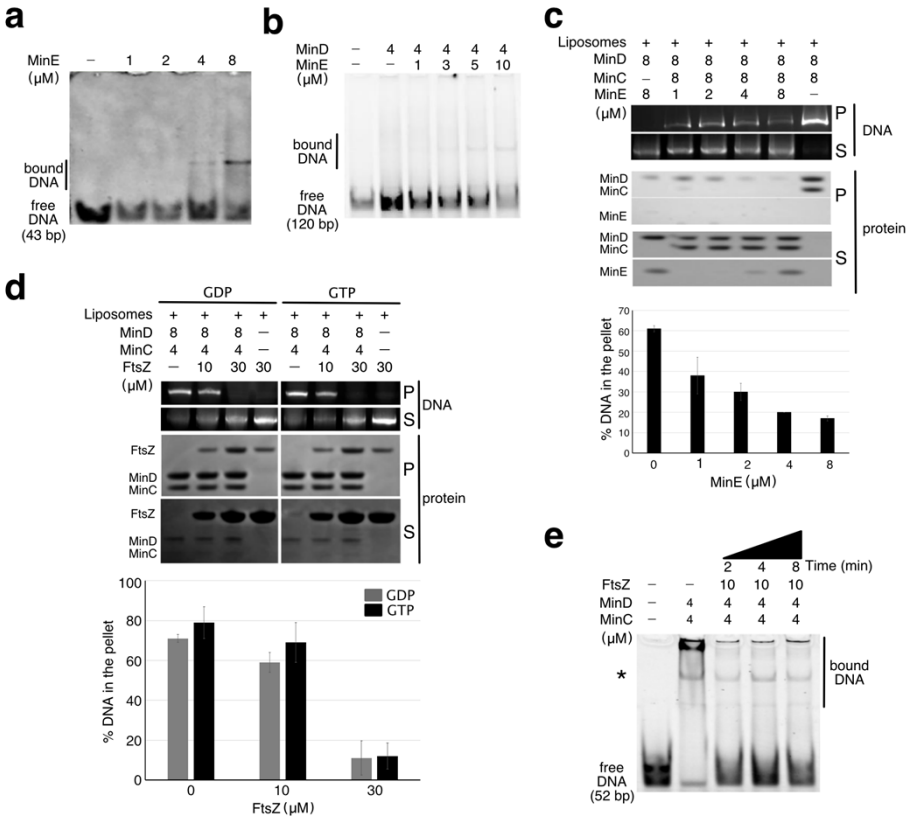

Fig 3. MinE and FtsZ interfere with DNA binding by the MinCD complex.

a-b, e Electrophoretic mobility shift assays (EMSAs) performed with the indicated proteins at the indicated concentrations, and HEX-labelled DNA of the indicated length. **c,d**, Liposome co-sedimentation assays. Upper panel, Gel-red-stained agarose gel used to visualize the DNA. Middle panel, Coomassie-stained polyacrylamide gel used to visualize the proteins. Lower panel, bar graph showing the quantification of the % of the DNA found in the pellet. Data represent mean ± S.E.M. of three (**c**) and two (**d**) independent experiments. In (**c**), the sample corresponding to 4 μM MinE was measured only once. S, supernatant. P, pellet. **e**, The time indicates the point at which FtsZ was added to the reaction. Total reaction time, 10 minutes. The asterisk indicates the height at which a band is visible, which is observed when incubating the DNA with MinD or MinC alone and does not represent binding by the MinCD complex.

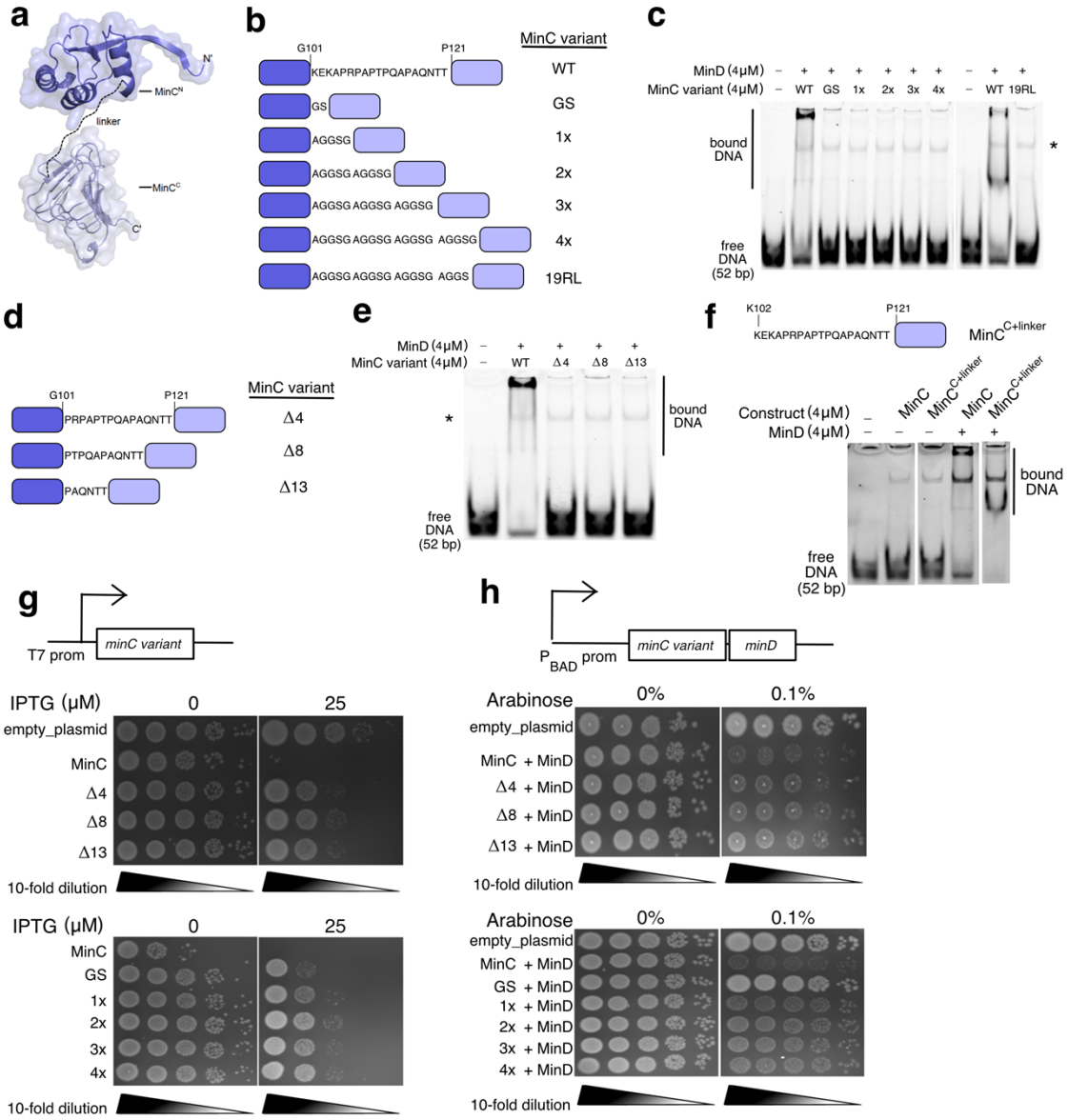

Fig 4. MinC linker is needed for DNA binding with MinD.

a, Modelled structure of *E. coli* MinC. Crystal structures of MinC N-terminal (PDB ID 4l1c) and C-terminal (PDB ID 5xdm) domains were obtained from the protein data bank (https://www.rcsb.org/). Linker, MinC linker region represented with a dashed line. **b,d,f** (upper panel), Schematics of the constructs. **c,e,f** (lower panel), Electrophoretic mobility shift assays (EMSAs) performed with the indicated proteins at the indicated concentrations, and HEX-labelled DNA of the indicated length. All reactions were performed in the presence of 1 mM ATP. **c,e**, Asterisk indicates the height at which a band is visible, which is observed when incubating the DNA with MinD or MinC alone and does not represent binding by the MinCD complex. **f**, lower panel, White lines indicate unrelated bands that were deleted from the image. The full image is shown in the Supplementary Fig. 5. **g,h**, Upper panel, Schematic of the promoter used in the experiment. Lower panel, representative image of

a plate onto which Rosetta BL21 (**g**) or MG1655ΔminB (**h**) cells transformed with the indicated constructs were spotted in a serial dilution. The experiment was repeated three times with similar results.

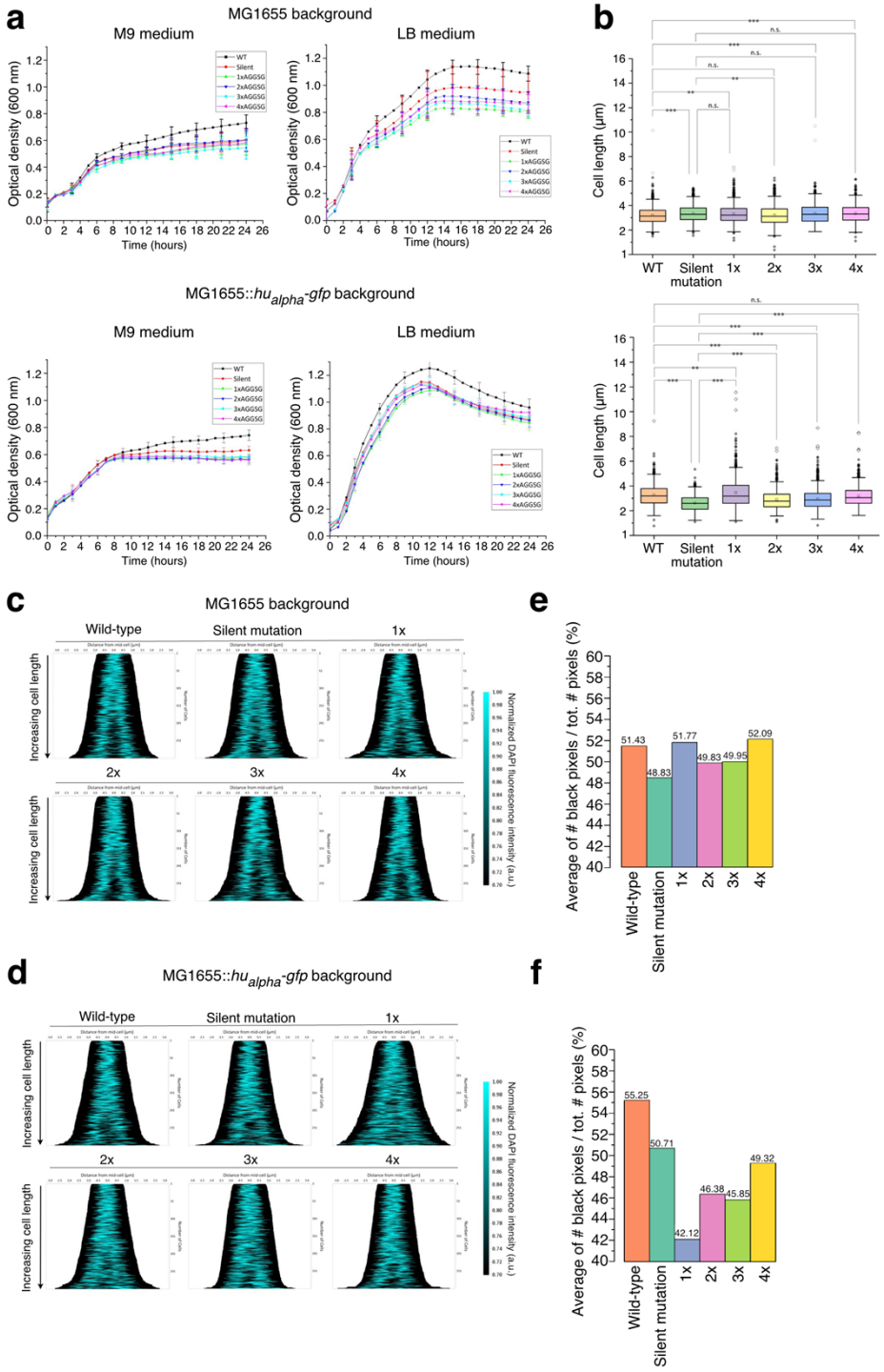

Fig 5. *E. coli* strains expressing MinC linker mutants from the endogenous locus show chromosome segregation defects.

919 **a,** Growth curves of the indicated strains in the indicated media. **b**, Graphs showing the quantification of the cell
920 length in the indicated strains. More than 500 individual cells were analyzed using the BacStalk software[48]. Shown
921 is the median with the first and third quartiles, as well as outliers. n.s., non-significant. *, p-value < 0.5. **, p-
922 value < 0.01. ***, p-value < 0.001. The p-value was calculated using the one-way ANOVA test. **c,d**, Demographs
923 of the DAPI signal measured via fluorescence microscopy in the indicated strains created with the MicrobeJ plugin
924 of ImageJ. **e,f**, Bar graph showing the average of the ratio between the number of black pixels and the total number
925 of pixels in the cell. **a-f**, Silent mutation, strain carrying four silent mutations in the linker region of MinC at the
926 chromosomal locus.
927
928
929
930
931
932
933
934
935

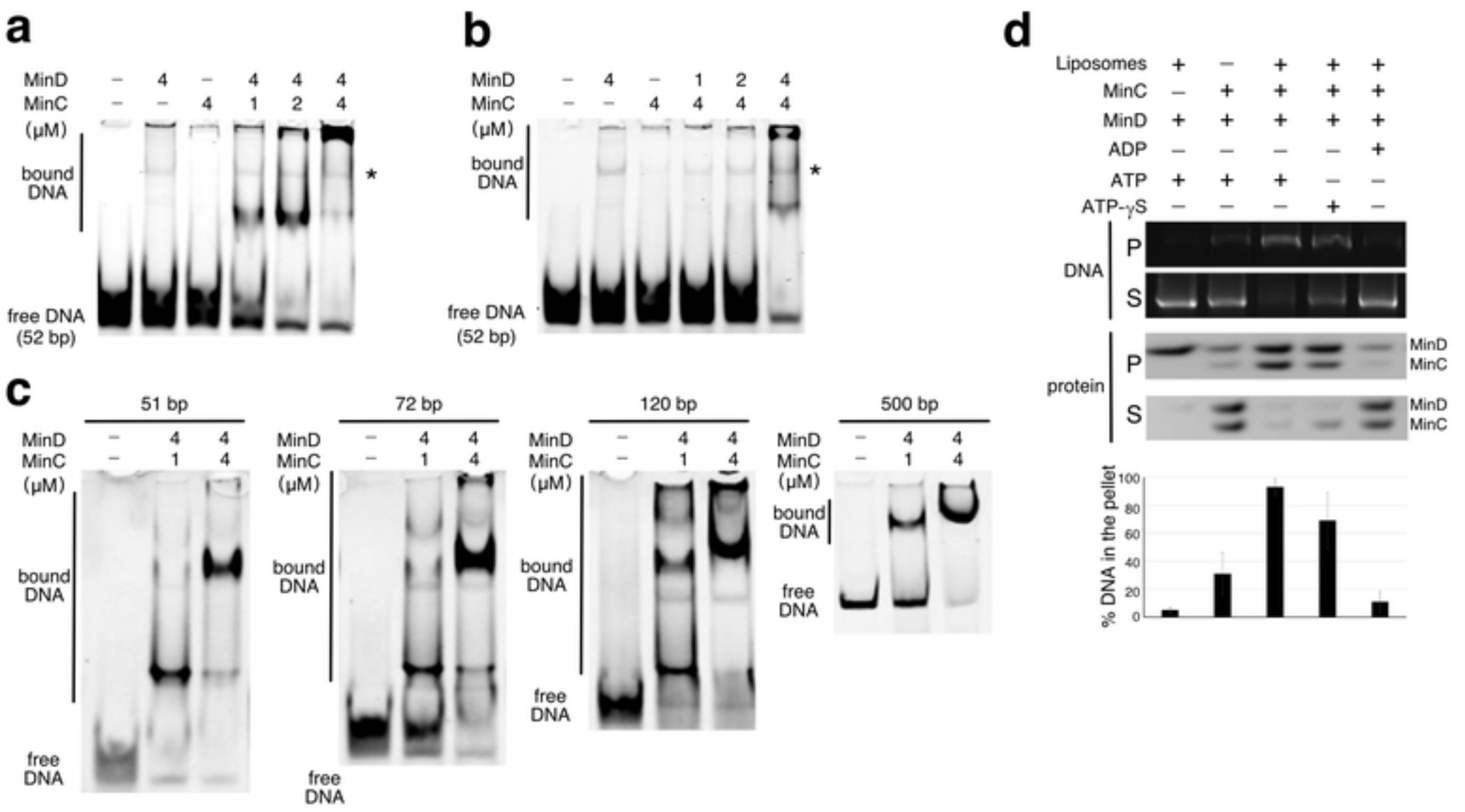
a
MinD – 4 – 4 4 4
MinC – – 4 1 2 4
(μM)
bound DNA
free DNA (52 bp)
*
b
MinD – 4 – 1 2 4
MinC – – 4 4 4 4
(μM)
bound DNA
free DNA (52 bp)
*
c
51 bp
72 bp
120 bp
500 bp
MinD – 4 4
MinC – 1 4
(μM)
bound DNA
free DNA
d
Liposomes + – + + +
MinC – + + + +
MinD + + + + +
ADP – – – – +
ATP + + + – –
ATP-γS – – – + –
DNA
P
S
protein
P
S
MinD
MinC
% DNA in the pellet
100
80
60
40
20
0

Figure 1

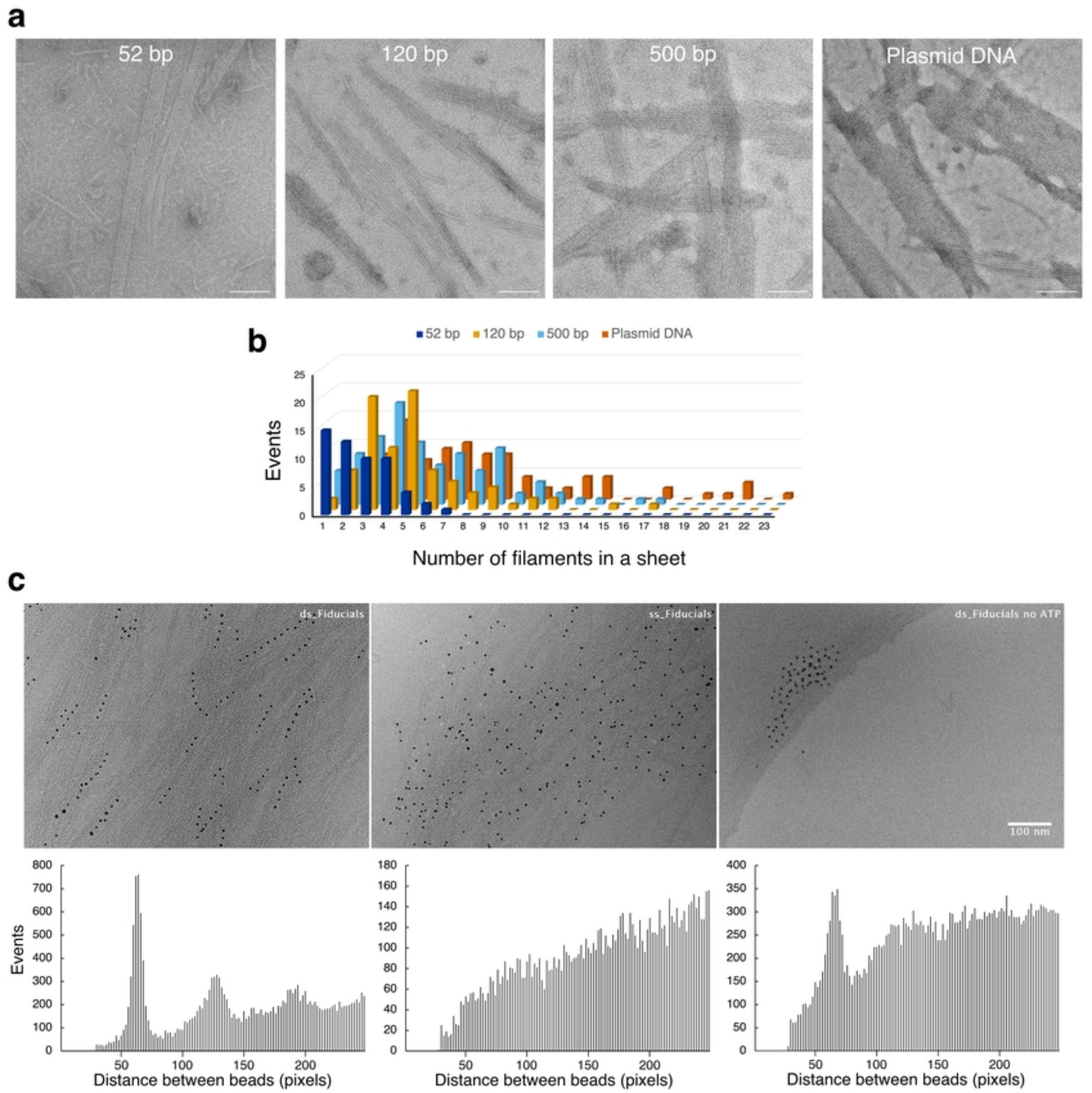
a
52 bp
120 bp
500 bp
Plasmid DNA
b
52 bp
120 bp
500 bp
Plasmid DNA
Events
Number of filaments in a sheet
c
ds_Fiducials
ss_Fiducials
ds_Fiducials no ATP
100 nm
Events
Distance between beads (pixels)
Distance between beads (pixels)
Distance between beads (pixels)

Figure 2

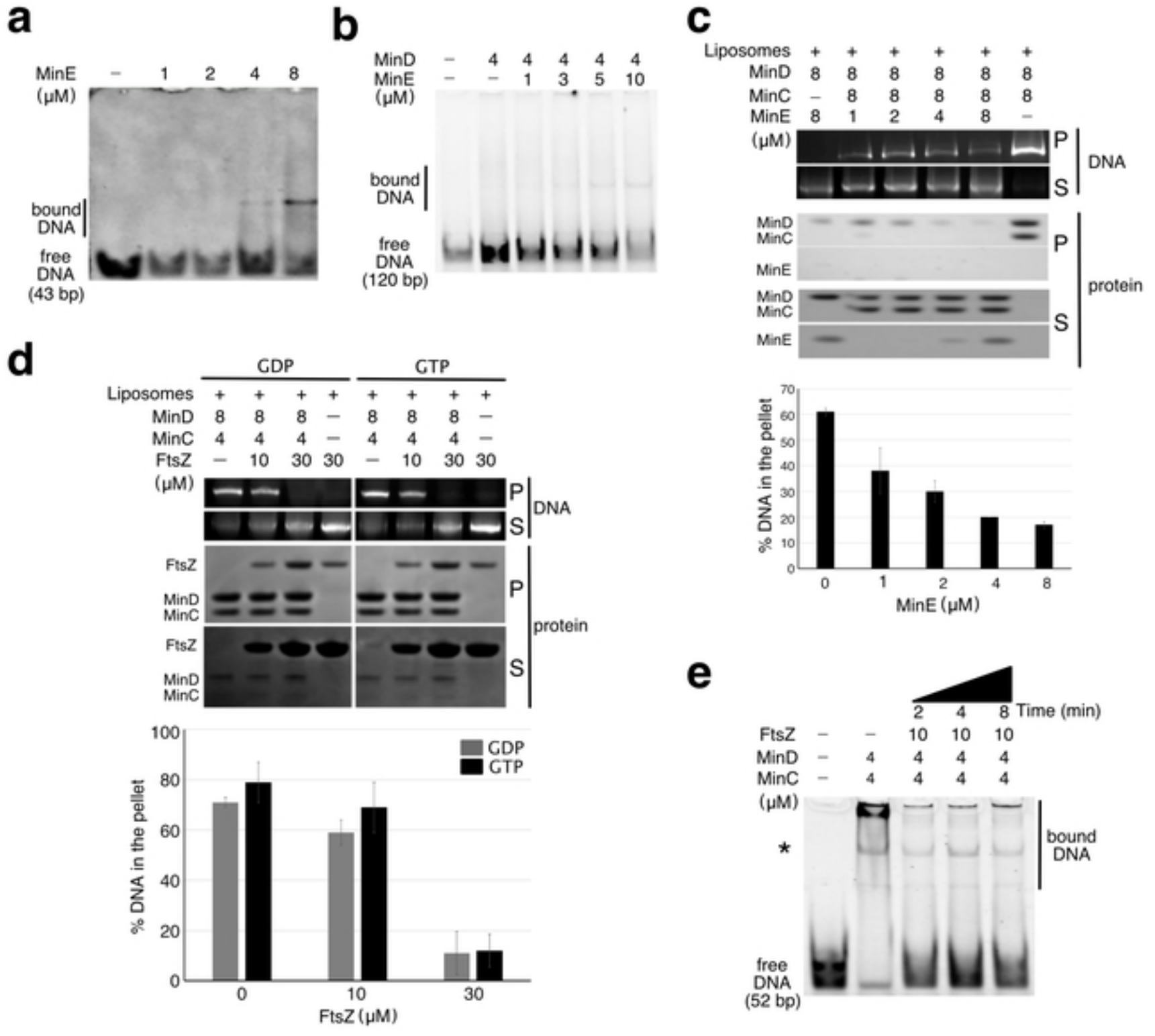
a
MinE (μM)
– 1 2 4 8
bound DNA
free DNA (43 bp)
b
MinD – 4 4 4 4 4
MinE – – 1 3 5 10
(μM)
bound DNA
free DNA (120 bp)
c
Liposomes + + + + + +
MinD 8 8 8 8 8 8
MinC – 8 8 8 8 8
MinE 8 1 2 4 8 –
(μM)
P
S
DNA
MinD
MinC
MinE
protein
% DNA in the pellet
MinE (μM)
d
GDP
GTP
Liposomes + + + + + + + +
MinD 8 8 8 – 8 8 8 –
MinC 4 4 4 – 4 4 4 –
FtsZ – 10 30 30 – 10 30 30
(μM)
DNA
FtsZ
MinD
MinC
protein
% DNA in the pellet
FtsZ (μM)
e
2 4 8 Time (min)
FtsZ – – 10 10 10
MinD – 4 4 4 4
MinC – 4 4 4 4
(μM)
*
bound DNA
free DNA (52 bp)

Figure 3

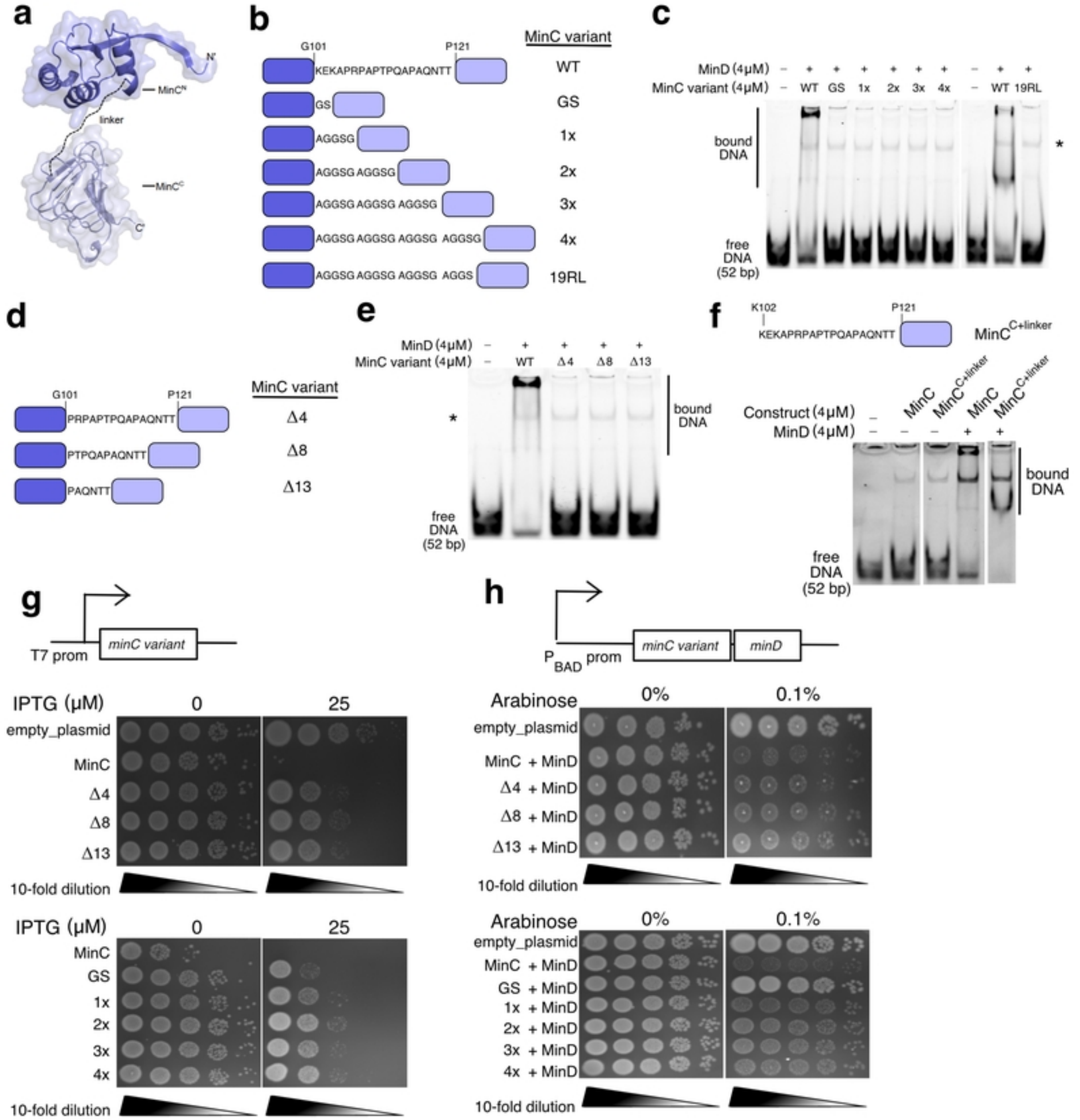
a
N
MinC^N
linker
MinC^C
C
b
G101
P121
KEKAPRPAPTPQAPAQNTT
GS
AGGSG
AGGSG AGGSG
AGGSG AGGSG AGGSG
AGGSG AGGSG AGGSG AGGSG
AGGSG AGGSG AGGSG AGGS
MinC variant
WT
GS
1x
2x
3x
4x
19RL
c
MinD (4μM)
MinC variant (4μM)
WT GS 1x 2x 3x 4x WT 19RL
bound DNA
free DNA (52 bp)
d
G101
P121
PRPAPTPQAPAQNTT
PTPQAPAQNTT
PAQNTT
MinC variant
Δ4
Δ8
Δ13
e
MinD (4μM)
MinC variant (4μM)
WT Δ4 Δ8 Δ13
bound DNA
free DNA (52 bp)
f
K102
P121
KEKAPRPAPTPQAPAQNTT
MinC^C+linker
Construct (4μM)
MinD (4μM)
MinC
MinC^C+linker
bound DNA
free DNA (52 bp)
g
T7 prom
minC variant
IPTG (μM)
0
25
empty_plasmid
MinC
Δ4
Δ8
Δ13
10-fold dilution
MinC
GS
1x
2x
3x
4x
h
P_BAD prom
minC variant
minD
Arabinose
0%
0.1%
empty_plasmid
MinC + MinD
Δ4 + MinD
Δ8 + MinD
Δ13 + MinD
10-fold dilution
GS + MinD
1x + MinD
2x + MinD
3x + MinD
4x + MinD

Figure 4

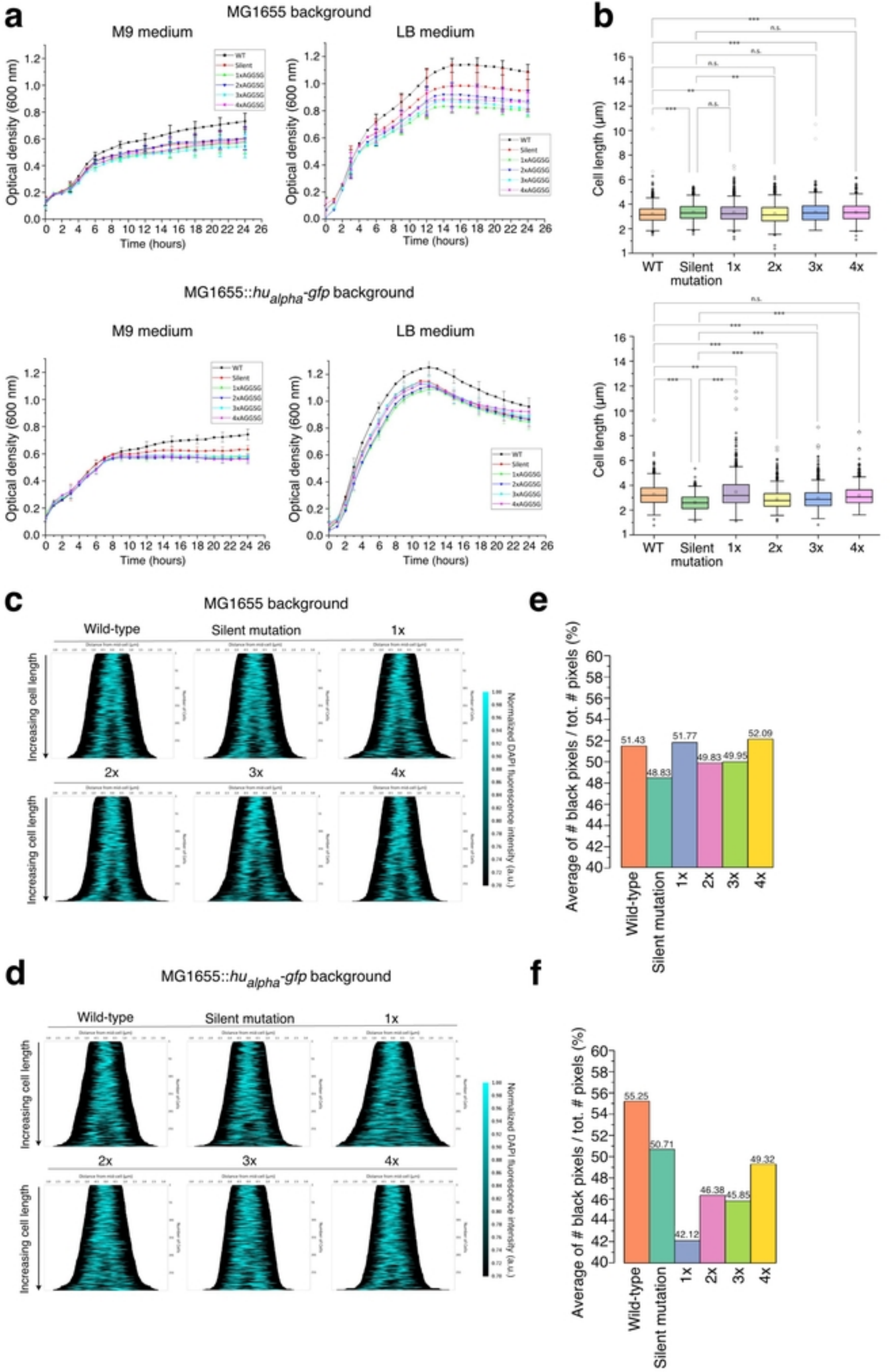
a
MG1655 background
M9 medium
LB medium
Optical density (600 nm)
Time (hours)
WT
Silent
1xAGGSG
2xAGGSG
3xAGGSG
4xAGGSG
MG1655::hu_alpha-gfp background
b
Cell length (µm)
WT
Silent mutation
1x
2x
3x
4x
n.s.
c
MG1655 background
Wild-type
Silent mutation
Increasing cell length
Normalized DAPI fluorescence intensity (a.u.)
d
MG1655::hu_alpha-gfp background
e
Average of # black pixels / tot. # pixels (%)
51.43
48.83
51.77
49.83
49.95
52.09
f
55.25
50.71
42.12
46.38
45.85
49.32

Figure 5